UAV Icing: Numerical Simulation of Icing Effects on Wing and Empennage

Markus Lindner
Ph.D. Student, Norwegian University of Science and Technology, UBIQ Aerospace, Trondheim, Norway

Joachim Wallisch
Ph.D. Student, Norwegian University of Science and Technology, UBIQ Aerospace, Trondheim, Norway

Richard Hann
Researcher, Norwegian University of Science and Technology, UBIQ Aerospace, Trondheim, Norway

Abstract

In-flight icing can result in severe aerodynamic performance penalties for unmanned aerial vehicles. It is therefore important to understand to which extent ice will build up on fixed-wing unmanned aerial vehicles wings and empennages, namely rudder and elevator, and how this ice will impact the aerodynamic performance and limits the flight envelope. This work investigates numerically icing effects on wing and empennage over a wide range of icing parameters. This is conducted using the icing CFD code FENSAP-ICE on the Maritime Robotics PX-31 Falk UAV. Therefore, the 2D profiles of these airfoils, which are RG-15 for the wing and SD8020 for rudder and elevator, are investigated. The investigated angles of attack are between $-5°$ and 14° in 0.5° increments. Furthermore, the icing conditions are chosen according to the FAA CS 25 Appendix C for continuous maximum and intermittent maximum icing. A broad range of temperatures, droplet median volumetric diameters, and the corresponding liquid water contents are simulated to generate a understanding of the icing effects according to Appendix C. An automation script to enable a more effective parallel execution of the in total 142 simulations of each airfoil has been used. The results of the simulations are used to calculate the change in the lift coefficient c_l, the drag coefficient c_d and the momentum coefficient c_m, and an estimate of the total accreted ice mass.
The aerodynamic performance penalties are strongly dependant on the environmental conditions. For both icing envelopes, two different worst case conditions are identified. For continuous maximum this condition lies at -2 °C and a droplet size of 15 µm, for intermittent maximum at -6 °C and 20 µm. For continuous maximum conditions the maximum lift can decrease by 37%, and the drag increase by 107%. For intermittent maximum the maximum lift can decrease by 35%, and the drag increase by 103%.

Introduction

Unmanned aerial vehicles (UAVs) have become increasingly attractive for military and commercial use over the last years. The Federal Aviation Administration (FAA) is projecting a growth of 40% over the next 5 years of remotely piloted UAVs in the USA [1]. To increase the availability of the UAV, the aircraft must be all-weather capable, especially in cold conditions. Atmospheric icing is a major hazard for UAVs and the research of this topic just recently gained attention [2]. It is therefore important to create knowledge to what extent in-flight icing affects the aerodynamic parameters of fixed-wing UAVs with wingspan of a few meters. Icing on aerodynamic surfaces of UAVs increases drag, decreases lift and the stall angle, and changes the mass of the aircraft [3, 4]. This results in decreased operational endurance and range. If no action is taken, icing can lead to dangerous behavior in flight, up to the loss of the aircraft [5]. UAVs with operations beyond the visual line of sight and autonomously operated UAVs are especially prone to dangerous icing conditions [3]. The pilot can not directly evaluate the weather conditions and can not assess if icing conditions exist in this moment without the aid of sensors. Furthermore, UAV wings and empennages are especially sensitive to icing compared to larger, manned aircraft [3].

For manned aviation, different types of ice protection systems (IPS) have been developed [6]. However, due to limitations in size, weight, and available energy those systems cannot be adapted to UAVs that are much smaller than commercial airliners [7]. IPS for these kinds of UAVs are in development, but not generally in use [8]. Therefore, small fixed-wing UAVs are usually not deployed in weather conditions where icing is probable.

In-flight icing occurs when supercooled liquid water hit the surfaces of an aircraft during flight and freeze, depending on the air temperatures, on or shortly after the impact on the surfaces [2]. Supercooled liquid water appears as cloud droplets or precipitation when the air temperature is below 0 °C but the droplets are still present in liquid form [2]. Icing conditions can occur almost all over the world at any time of the year [9, 10] which has a significant influence on the availability of UAVs without ice protection system. In Nordic countries like Norway icing conditions can inhibit UAV operations for more than 100 days a year [11].

For in-cloud icing there are different variables that describe the icing environment: the liquid water content (LWC), the droplet median volumetric diameter (MVD), the ambient air temperature, and the relationship between them [12]. Appendix C of the FAA Code of Federal Regulations 14 CFR Part 25 [12] connects these variables as worst case conditions for the certification process. Furthermore, Appendix C distinguishes between continuous maximum icing (CM) and intermittent maximum icing (IM). In this work both conditions are investigated.

Depending on the air temperature, different ice shapes are formed on the surfaces of the aircraft with varying properties regarding the influence on the aerodynamics. Examples for the different ice shapes can be found in Fig. 1. The most common are rime, glaze, and mixed ice. Rime ice occurs at cold temperatures where the droplets freeze immediately on impact [13]. Thereby the ice encloses small air pockets and therefore appears white [2]. The immediate freezing of the droplets leads to the generation of airfoil-like ice shapes and

results in the least aerodynamic penalties compared to other ice shapes.
Glaze ice forms at negative temperatures close to the freezing temperature. It is typically characterized by the formation of horn-like structures which result in significant aerodynamic penalties [14]. These penalties are caused by the shape of the horn and the separation of the flow behind the structure which will reattach only much further downstream of the airfoil [13]. Droplets impinging on the airfoil do not freeze immediately but a thin water film will build up on the surface and will freeze eventually [2]. No air bubbles are enclosed and therefore, the ice appears translucent. Mixed ice is a combination of glaze and rime ice. The temperature is higher than for rime, but lower than the temperature for glaze. The generated shapes can vary considerably and even produce horn structures.

The aim of this work is to analyze the effect of icing on wing and empennage of fixed-wing UAVs with a wingspan of few meters. The airfoil profiles considered for this investigation are taken from the Maritime Robotics PX-31 Falk. The Falk is a battery powered small UAV with a wingspan of 3.2 m and a maximum take-off weight of 25.0 kg [15]. The UAV is depicted in Fig. 2. The cruise speed of 25 m/s is used as air speed for the simulations in this work.

To analyze the icing effects, 2D wing and empennage profiles are simulated using computational fluid dynamics (CFD). The utilized software ANSYS FENSAP-ICE combines CFD simulations with icing simulations and is used to calculate the ice shapes and the aerodynamic parameters lift coefficient c_l, drag coefficient c_d, and momentum coefficient c_m. Furthermore, the accreted ice mass for wing and empennages are estimated. This works investigates the icing conditions stated in Appendix C by looking at a large number of LWC, MVD, and temperature combinations. Thereby, the complete Appendix C envelope for CM and IM icing conditions is covered. An automation script for FENSAP-ICE is used to enable this huge number of simulations. This work demonstrates the dangers of in-flight icing on fixed-wing UAVs and helps UAV designer and operator to understand the significance of this topic regarding aerodynamic parameters and added weight. The investigation of the complete icing envelope gives an overview of the most critical conditions for wing, rudder, and elevator. The designer are thereby able to evaluate their UAV in regards to sensitivity to icing and can be used for considerations for an ice protection system.

Similar studies have been conducted by [4] and [16]. In [4] the authors conduct a comparable study of 16 environmental conditions of Appendix C CM using FENSAP-ICE. The investigated airfoil is RG-15 with a chord length of 0.45 m and the accretion is simulated at an angle of attack of 0°. The results show that the worst conditions can be found close to the freezing temperature and a droplet size of 20 µm.
In [16] the authors compare numerically and experimentally generated ice shapes and performance penalties to each other. In this study three different temperature have been investigated. The ice shapes are simulated using LEWICE, the performance penalties are evaluated using FENSAP-ICE. The performance penalties are traced back to the shape of the accumulated ice. The accuracy between situational and experimental performance parameters depends on the extend of the decrease in performance with less agreement for stronger performance penalties.

Methods

Investigated Cases
The ice shapes are generated using icing CFD. Conducting icing simulations on large objects is costly regarding computational resources and therefore, only the airfoil profiles of the mean

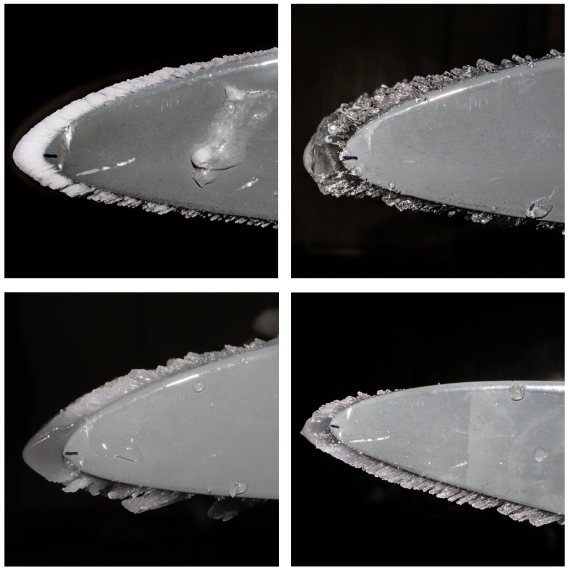

Figure 1: Different ice types (clockwise, starting top left): rime ice, glaze ice, mixed ice at high angle of attack and mixed ice from [3].

Figure 2: Maritime Robotics PX-31 Falk from [15]

aerodynamic chord of the wing and horizontal and vertical stabilizer are simulated. These respective mean aerodynamic chords are used to calculate the accreted ice mass for the whole wing and the hole empennage. In this work the influence of the taper ratio and the corresponding change of the chord length in wingspan direction and 3D effects are neglected. At low flight speeds no strong 3D effects are expected but are planed to be expected further in the future [17]. The sweep angle is 13.6° and the taper ratio 0.57. The airfoil profiles are RG-15 for the wing and SD8020 for rudder and elevator. The chord-lengths are 0.27 m, 0.25 m, and 0.20 m for the wing, elevator and rudder, respectively 5.
In this paper, 142 different environmental conditions are simulated. They are composed of nine different temperatures for CM and eleven temperatures for IM. Thereby, the three ice types rime, mixed, and glaze ice are produced. Furthermore, the icing conditions are chosen according to the FAA CS 25 Appendix C for CM and IM icing.
To conduct a full investigation of Appendix C CM and IM, six different MVDs for CM and eight for IM are simulated. IM includes colder temperatures and bigger droplet sizes. The used MVDs and the corresponding liquid water content, which is dependent on the air temperatures, are depicted in Tab. 1 and Tab. 2 for CM and in Tab. 3 and Tab. 4 for IM.
The ice accretion of the elevator and the wing is simulated for an angle of attack (AOA) of 4° for all environmental conditions. In this paper a change of the AOA during the ice accretion period due to the iced airfoil surface and the adaption of the UAV to higher AOAs due to reduced lift and increased ice mass is not examined. After the ice

	15 µm	20 µm	25 µm
−2 °C	0.76 g/m^3	0.60 g/m^3	0.46 g/m^3
−4 °C	0.72 g/m^3	0.55 g/m^3	0.42 g/m^3
−6 °C	0.68 g/m^3	0.51 g/m^3	0.38 g/m^3
−8 °C	0.64 g/m^3	0.47 g/m^3	0.34 g/m^3
−10 °C	0.60 g/m^3	0.44 g/m^3	0.31 g/m^3
−15 °C	0.45 g/m^3	0.32 g/m^3	0.23 g/m^3
−20 °C	0.30 g/m^3	0.21 g/m^3	0.15 g/m^3
−25 °C	0.25 g/m^3	0.17 g/m^3	0.12 g/m^3
−30 °C	0.20 g/m^3	0.14 g/m^3	0.10 g/m^3

Table 1: LWC according to Appendix C CM for different temperatures and MVD up to 25 µm.

	30 µm	35 µm	40 µm
−2 °C	0.35 g/m^3	0.24 g/m^3	0.14 g/m^3
−4 °C	0.32 g/m^3	0.22 g/m^3	0.13 g/m^3
−6 °C	0.28 g/m^3	0.20 g/m^3	0.12 g/m^3
−8 °C	0.25 g/m^3	0.18 g/m^3	0.11 g/m^3
−10 °C	0.22 g/m^3	0.15 g/m^3	0.10 g/m^3
−15 °C	0.17 g/m^3	0.12 g/m^3	0.08 g/m^3
−20 °C	0.11 g/m^3	0.08 g/m^3	0.06 g/m^3
−25 °C	0.09 g/m^3	0.06 g/m^3	0.05 g/m^3
−30 °C	0.07 g/m^3	0.05 g/m^3	0.04 g/m^3

Table 2: LWC according to Appendix C CM for different temperatures and MVD larger than 25 µm.

	15 µm	20 µm	25 µm	30 µm
−2 °C	2.81 g/m^3	2.47 g/m^3	1.70 g/m^3	1.27 g/m^3
−4 °C	2.74 g/m^3	2.41 g/m^3	1.64 g/m^3	1.21 g/m^3
−6 °C	2.66 g/m^3	2.35 g/m^3	1.58 g/m^3	1.15 g/m^3
−8 °C	2.58 g/m^3	2.29 g/m^3	1.52 g/m^3	1.09 g/m^3
−10 °C	2.50 g/m^3	2.23 g/m^3	1.46 g/m^3	1.03 g/m^3
−15 °C	2.21 g/m^3	1.97 g/m^3	1.31 g/m^3	0.92 g/m^3
−20 °C	1.92 g/m^3	1.71 g/m^3	1.15 g/m^3	0.82 g/m^3
−25 °C	1.52 g/m^3	1.35 g/m^3	0.93 g/m^3	0.67 g/m^3
−30 °C	1.11 g/m^3	0.99 g/m^3	0.71 g/m^3	0.51 g/m^3
−35 °C	0.68 g/m^3	0.60 g/m^3	0.43 g/m^3	0.30 g/m^3
−40 °C	0.25 g/m^3	0.21 g/m^3	0.15 g/m^3	0.10 g/m^3

Table 3: LWC according to Appendix C IM for different temperatures and MVD up to 30 µm.

accretion a performance sweep is conducted at a temperature of 0 °C to make the cases comparable to each other. For each of these two airfoils 39 different AOAs between −5° and 14° are investigated in 0.5° increments.
The rudder is investigated differently. Due to its vertical orientation in regard of the UAV the ice accretion is done for an AOA of 0° and 0° of yaw angle. The influence of change in AOA is neglected in this case. Therefore, now AOA sweep is conducted and only one data set of c_l, c_d, and c_m is produced for each environmental condition.
The investigated icing times are 21.5 min and 200 s for CM and IM, respectively. Appendix C specifies cloud sizes for CM and IM, which are 17.4 NM for CM and 2.6 NM for IM. An aircraft flying with 25 m/s requires this time to cross those clouds. Table 5 gives an overview over the selected settings.

Simulation Setup
The CFD simulations are conducted with ANSYS FENSAP-ICE version 2022 R2. FENSAP-ICE consist of three modules: FENSAP, DROP3D and ICE3D. FENSAP calculates the airflow around the airfoil by solving the Reynolds-averaged Navier-Stokes equations (RANS) numerically [18]. The utilized turbulence model in this work

	35 µm	40 µm	45 µm	50 µm
−2 °C	0.95 g/m^3	0.71 g/m^3	0.53 g/m^3	0.38 g/m^3
−4 °C	0.89 g/m^3	0.66 g/m^3	0.50 g/m^3	0.36 g/m^3
−6 °C	0.83 g/m^3	0.61 g/m^3	0.46 g/m^3	0.34 g/m^3
−8 °C	0.77 g/m^3	0.56 g/m^3	0.42 g/m^3	0.32 g/m^3
−10 °C	0.71 g/m^3	0.51 g/m^3	0.39 g/m^3	0.30 g/m^3
−15 °C	0.64 g/m^3	0.45 g/m^3	0.33 g/m^3	0.24 g/m^3
−20 °C	0.57 g/m^3	0.39 g/m^3	0.27 g/m^3	0.18 g/m^3
−25 °C	0.47 g/m^3	0.32 g/m^3	0.22 g/m^3	0.14 g/m^3
−30 °C	0.36 g/m^3	0.25 g/m^3	0.16 g/m^3	0.10 g/m^3
−35 °C	0.22 g/m^3	0.15 g/m^3	0.11 g/m^3	0.07 g/m^3
−40 °C	0.07 g/m^3	0.06 g/m^3	0.05 g/m^3	0.05 g/m^3

Table 4: LWC according to Appendix C CM for different temperatures and MVD larger than 25 µm.

	Wing	Elevator	Rudder
Profile type	RG-15	SD8020	SD8020
chord length c	0.27 m	0.25 m	0.20 m
Angles of attack	−5° ... 14°		
Icing time t_{ice}	1290 s for CM and 200 s for IM		
Free stream velocity	25 m/s		
Static air pressure p	101325 Pa		
Angle of attack for ice accretion	4°		
Turbulence model	Menter k-ω-SST, fully turbulent		
Roughness height	0.0005 m		

Table 5: Simulation settings

is the Menter k-ω-SST, run fully turbulent. DROP3D is a 3D eulerian water droplet impingement module [19]. It is used to calculate, among others, water concentration, droplet velocity vectors, water catch efficiency distributions and impingement limits [20]. ICE3D determines ice accretion, water runback and gives as results the ice shape, water film thickness and the surface temperature [20, 21]. After the ice shape has been generated, a remeshing step of the flow field is conducted. The remeshing tool is also part of ICE3D and includes different grid displacement methods. In this work the remeshing is done by Fluent Meshing, since it allows the user to set the remeshing parameters more precisely.
In this paper multishot simulations are used [22]. The simulated icing times of 1290 s and 200 s for CM and IM, respectively, are divided into fifteen and thirteen steps. To generate the ice roughness, the first step simulates 30 seconds of icing for CM and 8 s for IM. The remaining steps are of equal length of 90 s for CM and 16 s for IM. The different simulated times for CM and IM are chosen to enable a comparison of the amount of water that impinges on the airfoils.
For the first timestep the roughness has been set to an uniform sand-grain roughness of 0.0005 mm. For the following timesteps the beading model has been used to calculate the surface roughness. In Appendix C the beading height of one CM case at −10 °C and 15 µm MVD can be found.
An automation script is used to enable an automatic execution of the large amount of simulations. Usually, FENSAP-ICE requires the user to setup a new simulation for every multishot icing simulation, regardless if he wants to investigate a new AOA, different temperature or LWC. The automation script gives the user the potential to specify different simulation cases within a text file and run them in parallel. Furthermore, the automation script executes automatically a performance simulation to investigate the aerodynamic performance.

Grid setup
For each of the three wing profiles a grid has been generated. These grids have been created based on [4]. This paper lists settings for the creation of a numerical grid for icing simulations and aerodynamic performance simulations of the iced airfoil after the ice has been created. Furthermore, a grid dependency study has been performed in

[4]. The grids used in this work is based thereon. The meshing has been done with the software Pointwise V18.6R1.
The grid is configured as a hybrid O-grid. The cells close to the wall are structured to enable a boundary layer resolution. The first layer height is chosen according to achieve a Y+ value of 1. In total the structured mesh consists of 35 layers with a growth rate of 1.15. In the farfield the mesh is unstructured. A detail of the mesh close to the leading edge of the wing profile can be found in Fig. 3.
Since FENSAP-ICE requires 3-dimensional cells the 2D grid is extruded for one cell in the y-direction. The width of the extrusion is 0.1 m which leads to a reference wing area of 0.027 m^2 for the wing, 0.025 m^2 for the elevator, and 0.020 m^2 for the rudder.
The remeshing settings in Fluent Meshing have been chosen to produce a grid that comes as close as possible to the original mesh created in Pointwise, whereat creating an identical mesh is not possible.

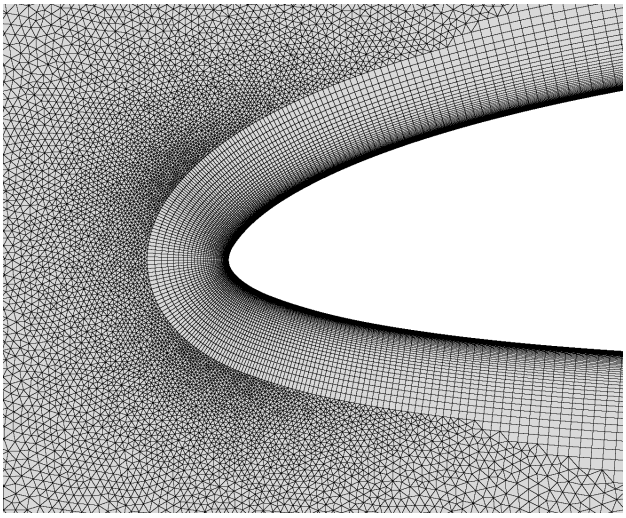

Figure 3: Mesh around the leading edge of the wing profile.

Grid study

A grid study has been conducted in this paper to evaluate the settings in regard to the amount of multishots and the size of the curvmin setting in the Fluent Meshing script. The evaluation has been done on the shape of the ice shapes since those settings have an impact on the shape itself and other evaluation parameters like c_l and c_d are influence by the shape of the accumulated ice. The simulations have been conducted on the wing airfoil at -2 °C and and AOA of 4°.
For the evaluation of the multishots, three different cases are investigated consisting of 7, 15, and 31 multishots. The length of the first shot is 30 s, the remaining shots are of equal length to achieve a total icing time of 1290 s. The resulting ice shapes are depicted in Fig. 4. The ice shape show to be strongly influence by the multishot settings, even though the upper and lower ice limits are the same for all three simulations. The lowermost number of shots displays a almost smooth shape. The ice thickness is smaller compared to the other simulations and a more deviating horn angle is found. The ice thickness of the simulations with 15 and 31 multishots show approximately the same ice thickness although the horn angles slightly differ. Compared to the 7 shots simulations those two consist of stronger developed horns on the leading edge. Only the 15 shots simulations exhibits small feathers at the lower surface.
For this paper 15 multishots have been selected. The reasons therefore are the small deviations to the 31 multishot simulation and the computational time.

The curvmin setting in Fluent Meshing sets the mesh sizes over wall surfaces and is important for the final shape of the accreted ice [23]. The size of curvmin is kept constant for the hole leading edge. The ice shapes with a variation in curvmin are depicted in Fig. 5. The general

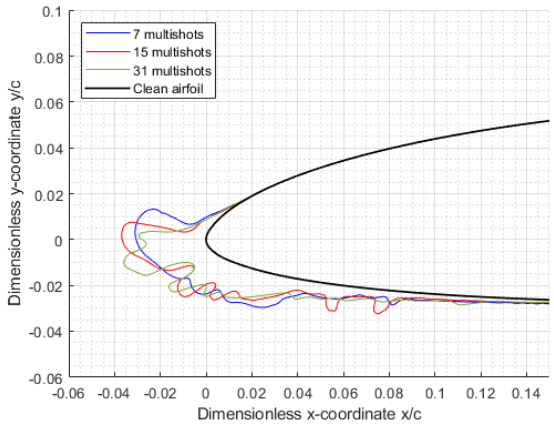

Figure 4: Study of the influence of different amount of multishots on the ice shape.

shape of the accumulated ice is barley influenced by this setting. E.g. the upper and lower ice limits stay the same. However, the two smallest settings - 0.0003 m and 0.00025 m - are able to capture small horns at the lower surface. Furthermore, the smallest curvmin setting shows a slightly different horn angle while maintaining the approximately same ice thickness. Due to problems at the remeshing step of some simulations with the 0.00025 m setting, a curvmin size of 0.0003 m has been chosen.

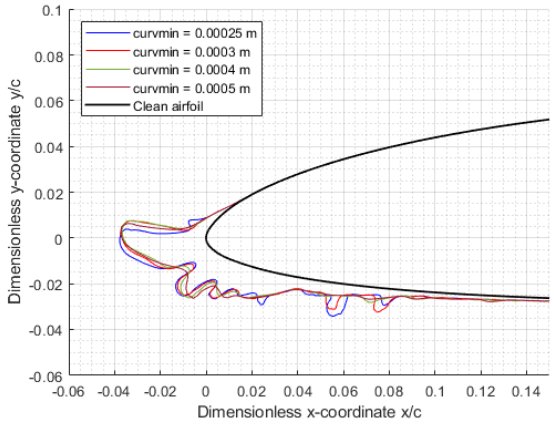

Figure 5: Study of the influence of the curvmin setting in Fluent Meshing on the ice shape.

Results

Ice accretion

This chapter looks at the ice accretion. Plots of the ice shapes and the accreted ice mass are presented.

Figures 6 and 7 show the ice shapes of the wing for CM and IM, respectively. For reasons of clarity not all ice shapes are depicted. A selection is chosen to visualize the change of a certain environmental parameter. The ice shapes of rudder and elevator can be found in the appendix.
The different environmental conditions have a significant impact on the shape of the accreted ice on the airfoil. The median volumetric diameter and the air temperature both have an influence on the ice shape and the accreted ice mass. Table 1, 2, 3, and 4 show a high

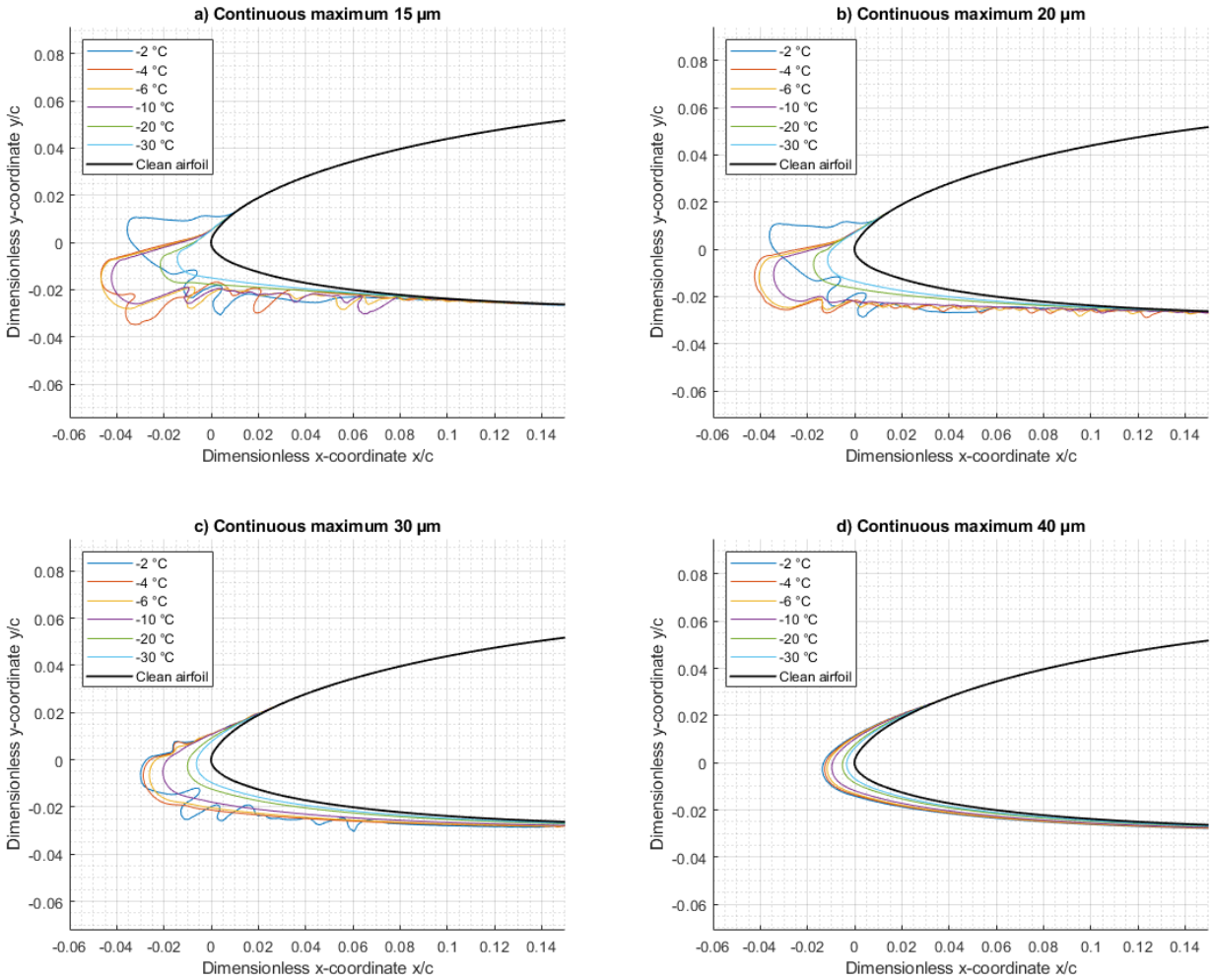

Figure 6: Wing ice shapes for CM conditions.

liquid water content for temperatures close to the freezing point and small median volumetric diameters in contrast to low LWCs at low temperatures and bigger MVDs. This results in more complex ice shapes in Fig. 6 a) , b), and c) compared to 6 d).

At first, the ice shapes of the CM conditions are analyzed in more detail. For a MVD of 15 µm the ice shapes show structures that can be interpreted as feathers. With decreasing temperatures these feathers become less pronounced and the accreted ice develops into a more streamlined shape. The temperatures −20 and −30 °C represent rime ice. The ice shape at the highest temperature −2 °C differs significantly from the other conditions. A distinct horn indicates that glaze ice is present. The remaining conditions can be described as mixed ice that differ in ice thickness.

With increasing droplet size, and the resulting decrease in LWC at the same temperature, the feathers become smaller. Rime ice is present at higher temperatures and glaze ice disappears completely for a MVD of 30 µm and larger droplets. Furthermore, the ice thickness decreases. For an MVD of 40 µm only rime ice is present. The ice shapes differ in ice thickness which can be traced back to higher LWC at higher temperatures.

Secondly, the intermittent maximum ice shapes are analyzed. Unlike the CM conditions, glaze ice is more prevailing. At high temperatures like −2 and −4 °C the high LWC causes the impinging water droplets to run back at the upper and lower side of the airfoil and freezing eventually. Therefore, the upper and lower ice limit shifts significantly backwards in chord direction. With decreasing temperatures the ice thickness increases and the ice shapes develop more pronounced horn features. This applies for temperatures as low as −10 °C. Decreasing the temperatures further leads to more streamlined ice shapes that decrease in ice thickness.

An increase of the droplet size from 15 µm to 20 µm has no significant impact on the ice shape. The upper and lower ice limits move slightly further downstream, but the ice shape and thickness stay approximately the same. When increasing the MVD further this effect is reversed. The ice limits shift towards the leading edge and the ice thickness is decreased. The ice horns are less pronounced and can only be found for the temperatures −4 and −6 °C at an MVD of 30 µm. For MVDs of 50 µm the accreted ice has a streamlined shape.

The accretion of ice on wing and empennage adds weight to the aircraft. The aircraft has to produce more lift to stay airborne. Therefore, it is important to know how much mass will accumulate. Since the results in this paper are produced by 2D-simulations the figures display the ice mass per length unit. In a second step the ice mass of the whole UAV is estimated. Therefore, the ice mass per meter is extrapolated for the wing, elevator, and rudder span of the Maritime Robotics Falk and added up for every environmental condition. Those spans are 2.7 m for the wing span (excluding the fuselage), 0.2 m for the rudder, and 0.77 m for the elevator. Due to the design of the UAV, the masses of the rudder are considered twice. In this mass analysis the change in chord length of the wing is not considered.

In the creation of the data points of the elevator seven environmental conditions could not be produced due to numerical problems. In the following plots these data points have been left blank.

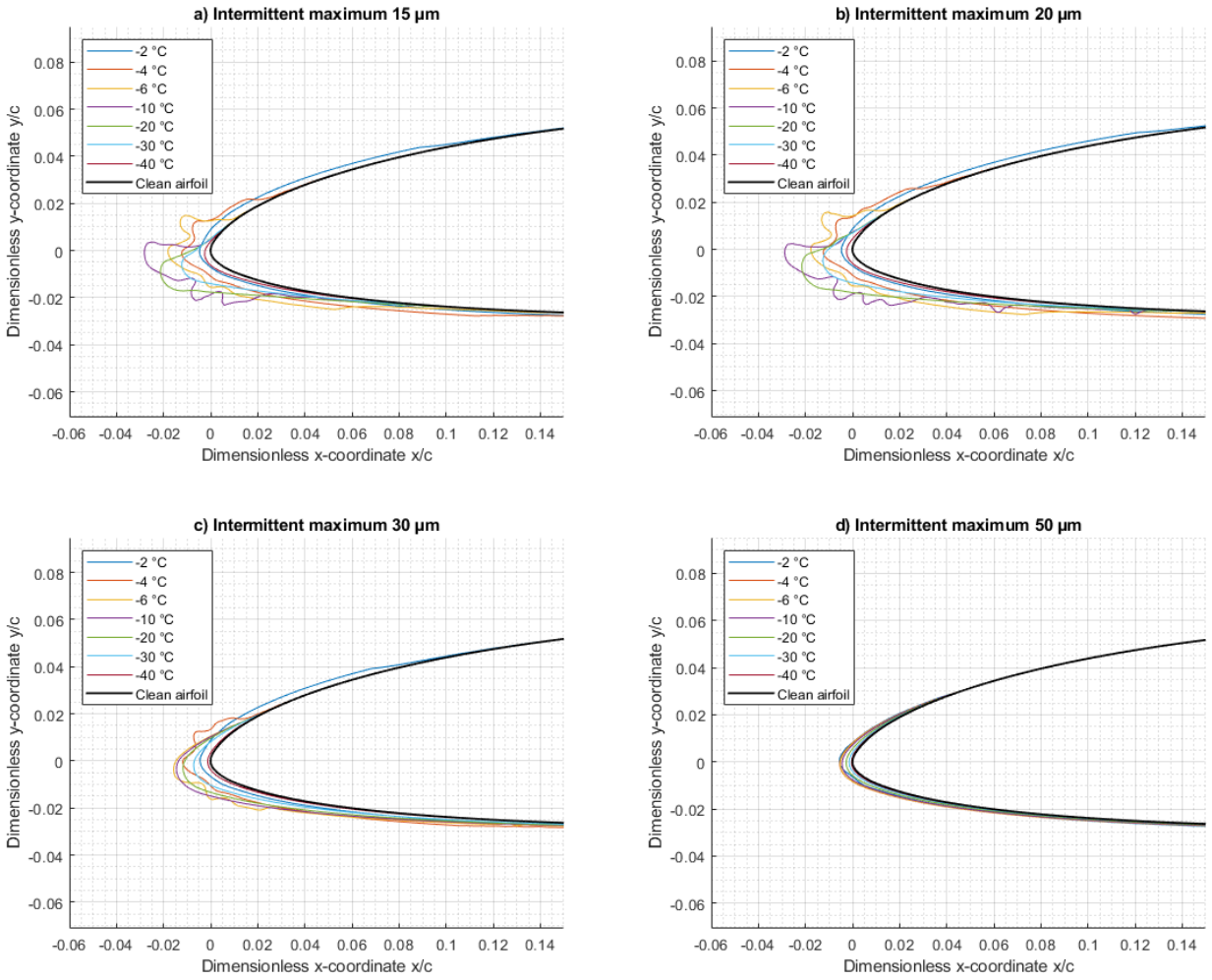

Figure 7: Wing ice shapes for IM conditions.

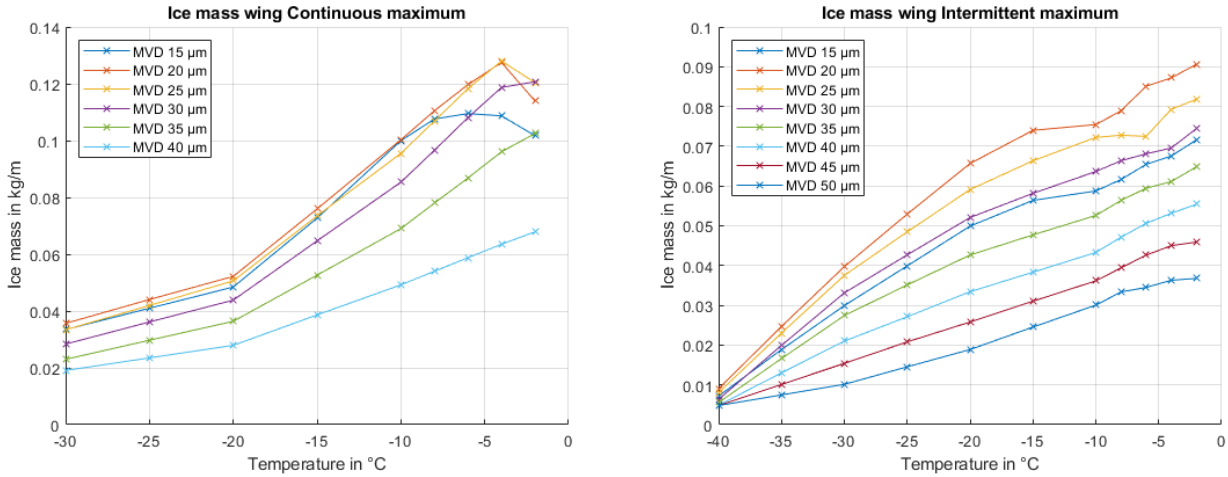

Figure 8: Mass of the accreted ice per length unit of the wing for CM and IM conditions.

The Figures 8 to 10 display the ice mass of the three investigated airfoils. The plots are divide into CM and IM for better presentation. Starting at the coldest temperature an increase in temperature leads for all environmental conditions to an increase in accumulated ice mass at first. Some CM conditions with small MVD - 15 µm, 20 µm, and 25 µm - achieve a peak ice mass at −4 °C and show a decrease in ice mass for −2 °C. The biggest ice masses for each temperature are achieved for MVDs of 20 µm, followed by 25 µm. Increasing the droplet size from 30 µm leads to an decrease in ice mass. The accreted ice mass is generally bigger for CM than IM despite the higher LWC. The reason therefor is probably the 6.5 times longer exposure time to icing conditions.

For CM conditions the biggest ice mass per length unit is 0.128 kg/m and is found for the wing at −4 °C and an MVD of 20 µm. The biggest ice mass for the wing under IM conditions is found at −2 °C and 20 µm with a value of 0.091 kg/m.

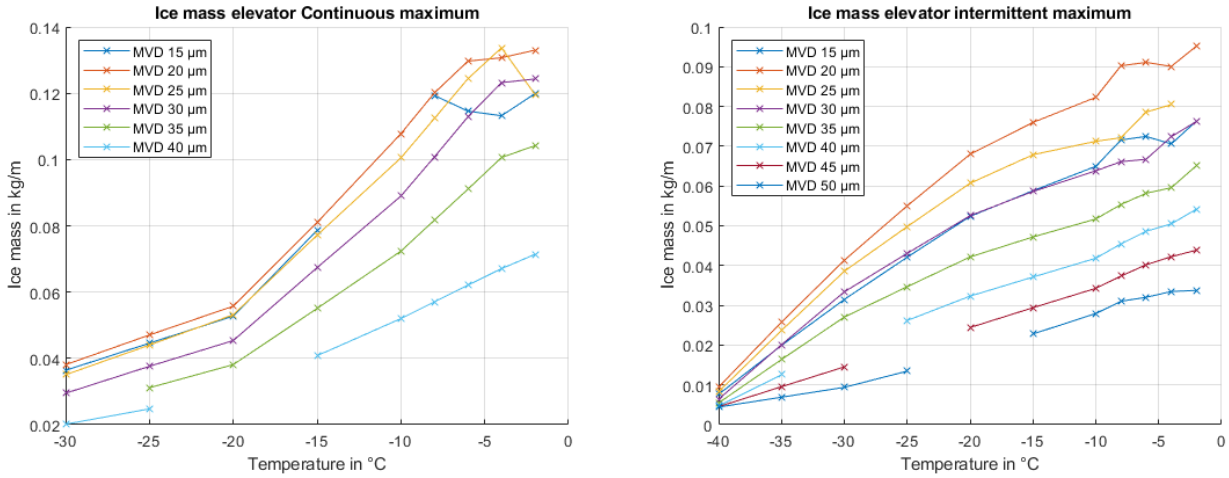

Figure 9: Mass of the accreted ice per length unit of the elevator for CM and IM conditions.

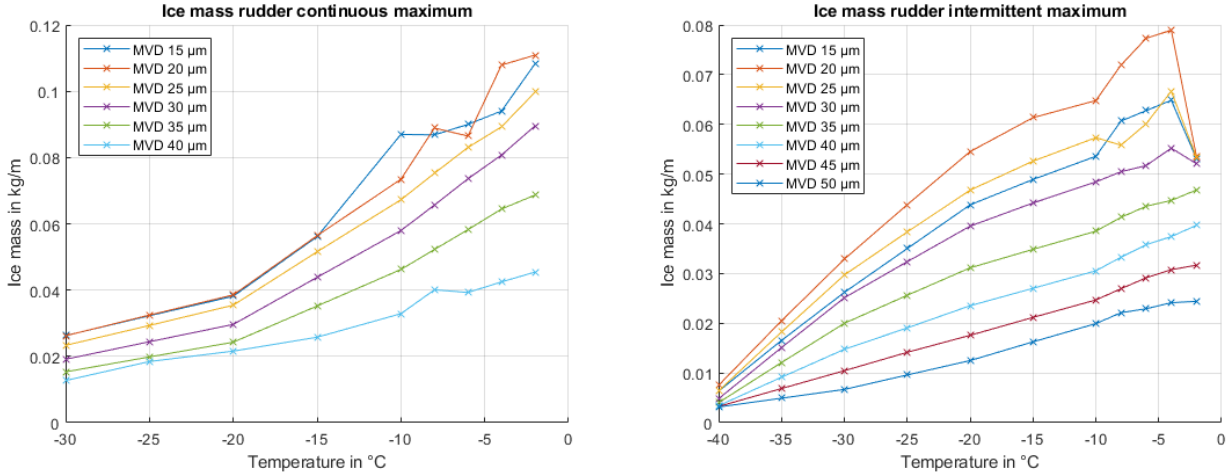

Figure 10: Mass of the accreted ice per length unit of the rudder for CM and IM conditions.

Figure 11 presents total ice mass of the UAV for CM and IM, respectively. The results reassure the observations of the 2D airfoils. CM conditions accumulate more ice mass than IM. The most ice is accreted for droplet sizes of 20 µm, followed by 25 µm. For CM conditions the biggest ice mass is 0.488 kg and is reached at -4 °C and an MVD of 20 µm. For IM conditions the biggest ice mass is reach at -2 °C and 20 µm with a value of 0.339 kg.

Performance

The previous chapter introduced ice shapes that are now evaluated regarding their aerodynamic performance. The investigated parameters therein are the stall angle, the reduction of lift, increase in drag and change in momentum coefficient.

Lift

Figure 12 depicts the lift coefficient c_l over the AOA α for the wing, six different MVDs and CM conditions. The stall angle of the clean airfoil is 11° and $c_{l,max}$ has a value of 1.22. A reduction in lift and stall angle is observable in all cases. Temperatures close to the freezing temperature exhibit the most significant performance degradation. The horn structures, that are depicted in Fig. 6 a) for a temperature of -2 °C - have the most severe impact on the aerodynamic parameters due to disattachment of the flow behind it. The droplet size of 25 µm at this temperature shows a reduction of 32% in stall angle to 7.5° and a reduction of 37% in maximum lift. With decreasing temperatures and therefore more streamlined ice shapes the aerodynamic penalties decrease. The reductions in stall angle and lift diminish to 5% and 9%, respectively. As shown previously an increase in droplet sizes leads to more streamlined ice shapes. This corresponds with less aerodynamic performance penalties which can be observed in Fig. 6 d) for an MVD of 40 µm. In this case the worst condition (e.g. -2 °C) exhibits a reduction of stall angle of 5% and 16% reduction in lift.
The aerodynamic performance losses differ slightly for IM conditions. The c_l-over-α plots are depicted in Fig. 13. Due to the more streamlined ice shapes close to the freezing temperature for small MVDs and IM conditions, the condition with the most performance degradation occurs at -6 °C and an MVD of 20 µm. The reduction of stall and maximum lift is 32% and 35%, respectively. This can be correlated to the appearance of horn structures at colder temperatures for IM than CM conditions.

Increasing the droplet size shifts the occurrence of the worst condition to -4 °C at 30 µm and -2 °C at 50 µm.

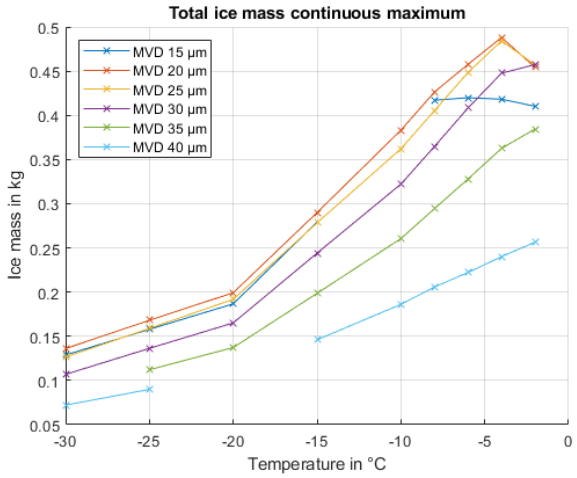

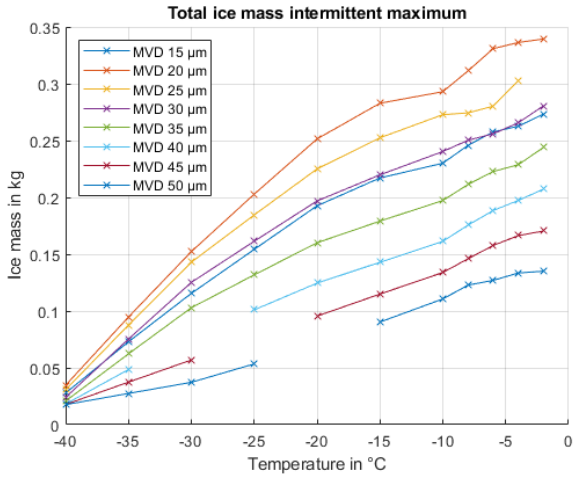

Figure 11: Total accumulated mass of the UAV for CM and IM conditions.

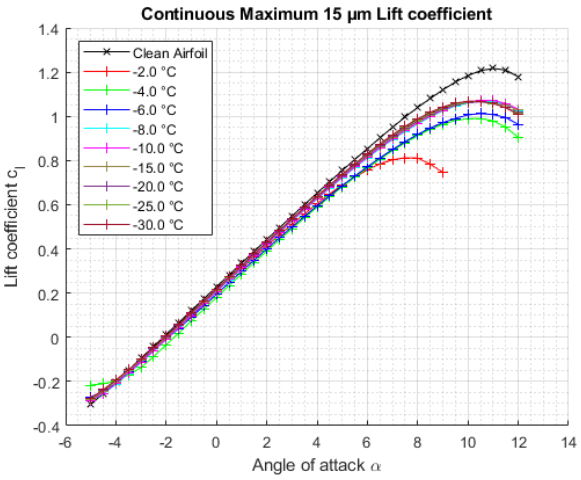

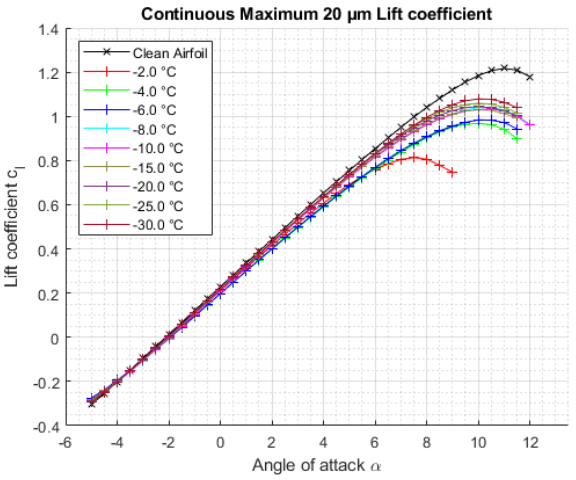

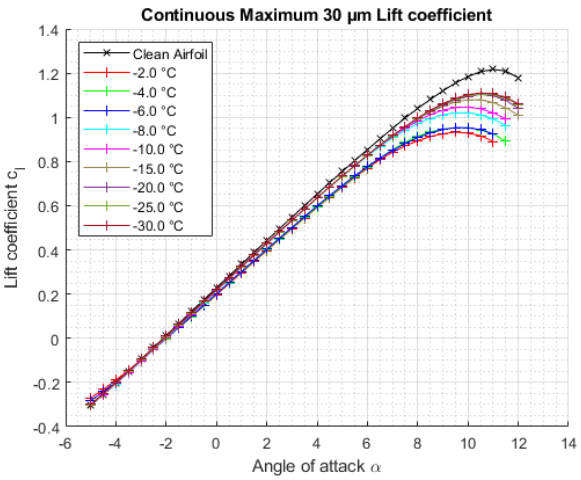

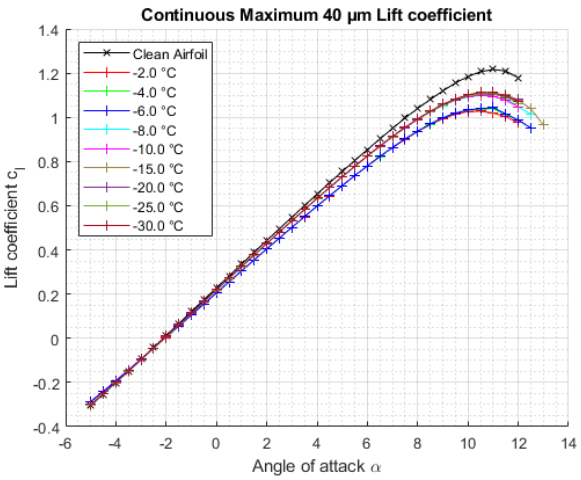

Figure 12: Lift coefficient c_l over the AOA α for the wing in CM conditions.

Drag

The influence of iced UAV airfoils on the drag coefficient is presented in Fig. 14 and 15. The performance degradation is compared against an angle of attack of 4°, since this is the AOA in normal flight conditions and the angle the ice accretion has been simulated on.

As already seen for the lift coefficient, temperatures close to the freezing temperature are impacting the aerodynamic parameters in CM conditions the most. The most severe increase in drag can be found at a temperature of -2 °C and an MVD of 15 µm. The drag increases by 107%. Furthermore, by increasing the AOA the drag curve exhibits a higher gradient. At the stall angle of the iced airfoil (e.g. 7.5° at -2 °C) the drag has risen by 227%. This increase in drag stays approximately the same for 20 µm and 25 µm. Increasing the

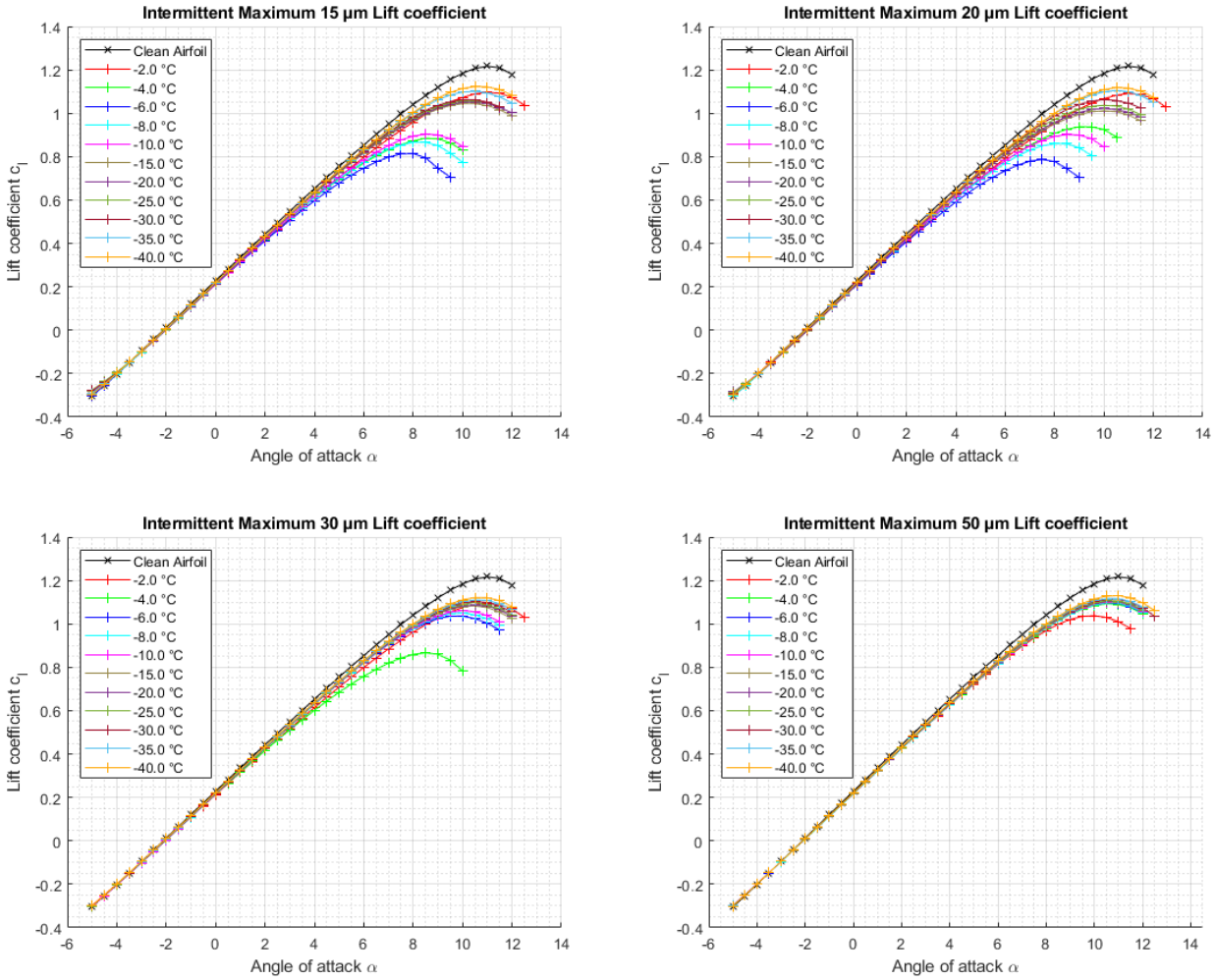

Figure 13: Lift coefficient c_l over the AOA α for the wing in IM conditions.

MVD further shows an decreased influence of the iced airfoil on the drag. At 40 µm the drag increases at the worst condition by 32%. The drag curves of the IM conditions behave similar to the lift curves. The largest increase in drag can be observed at a temperature of −6 °C. For an MVD of 20 µm the drag has increased by 103% for the evaluated AOA of 4°. Similar to CM conditions the drag rises steeper with increased AOA compared to the clean airfoil. At the stall angle the drag has increased by 221%.
The influence of an iced wing on the C_l-over-c_d-polar can be found in Appendix B.

Momentum

The momentum coefficients are depicted in Fig. 16 and 17. For every conditions, CM and IM, steeper momentum gradients are present. The most severely impacted conditions are like for lift and drag for CM −2 °C and −6 °C for IM at low LWC.

Icing Severity

To estimate the overall worst environmental icing condition for CM and IM, an analysis of the performance degradation due to icing is conducted. This study is adapted from [4]. Therefore, three parameters are evaluated: The degradation of $c_{l,max}$, offset in stall angle and drag at an AOA of 4°. Each environmental condition is given a value between 0 and 1 for the three parameters, in which 0 stands for the lowest, 1 for the highest negative impact on performance. The assigned value is relative to the lowest and highest degrading condition. After that, the average value of lift, stall, and drag degradation is calculated and again assigned a value between 0 and 1. The results of the severity analysis for the wing in CM and IM conditions are depicted in Fig. 19. The figure gives information about the most and least impacting environmental condition. For CM, the worst condition is at −2 °C and a MVD of 15 µm, for IM at −6 °C and 20 µm MVD. The least severe condition is found for CM at −15 °C and 40 µm MVD, for IM at −40 °C and a MVD of 40 µm. Fig. 33 depicting the icing severity for the elevator can be found in the appendix. For the elevator, the most and least impacted conditions slightly differ form the wing, but stay approximately in the same region. For CM, the worst condition is at −2 °C and a MVD of 20 µm, for IM at −8 °C and 20 µm MVD. The least severe condition is found for CM at −25 °C and 25 µm MVD, for IM at −40 °C and a MVD of 15 µm.

Elevator and Rudder

The stall angle, lift, drag, and momentum coefficients for the iced elevator show similar behavior than the wing. Therefore, they are not evaluated here in detail, but the plot can be found in the appendix.
The rudder of the Maritime Robotics Falk is installed perpendicular to the elevator and therefore not influenced by a change of AOA. Furthermore, the airfoil profile SD8020 has no camber. Plots of lift and momentum curves are therefore not interesting. The airfoil, however, contributes to the overall drag of the UAV. Figure 18 show the drag coefficient of the rudder for CM and IM conditions, respectively, and compare it to the clean airfoil. An increase in drag

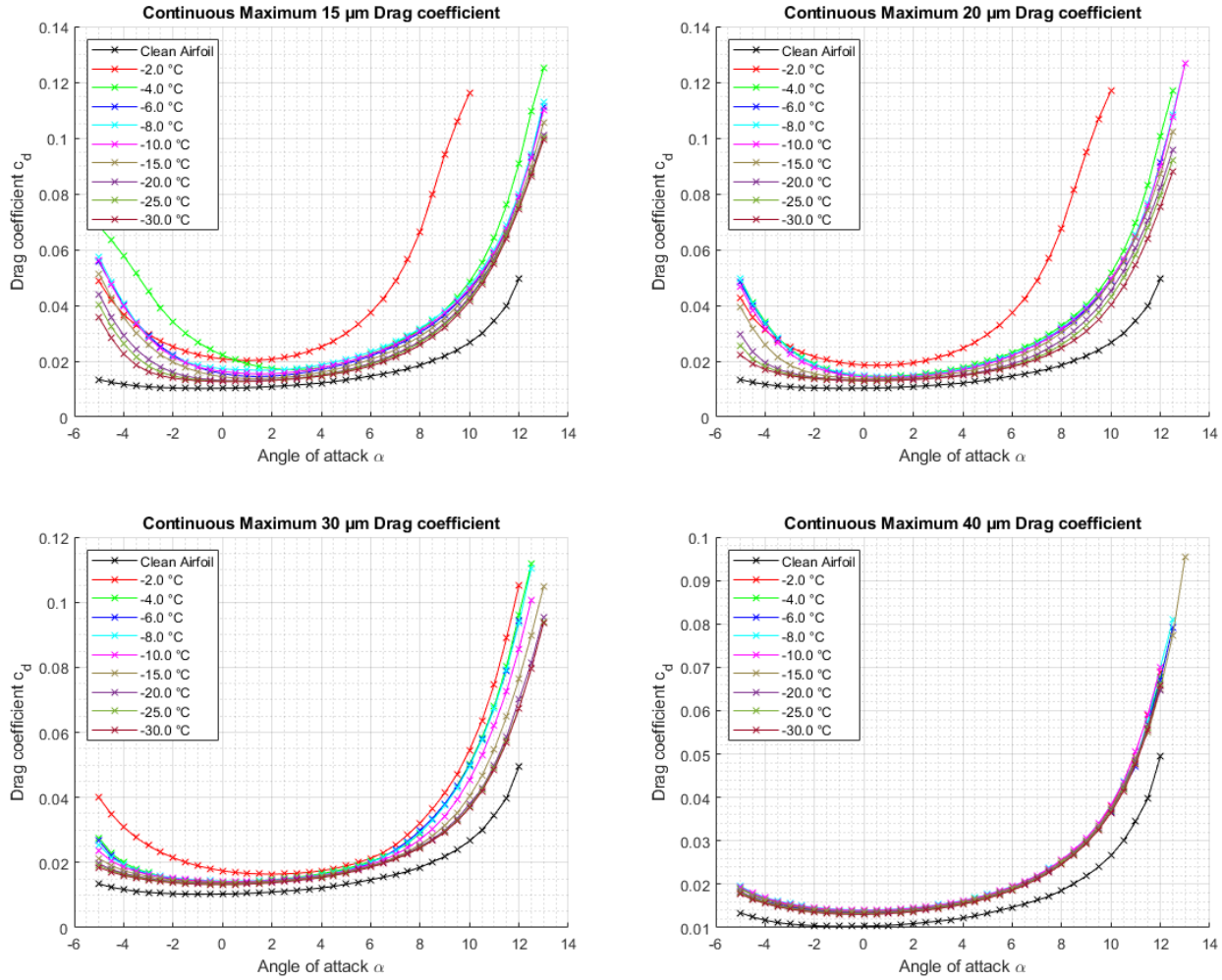

Figure 14: Drag coefficient c_d over the AOA α for the wing in CM conditions.

can be observed for all environmental conditions. As for the wing, the biggest increase in drag can be found close to the freezing temperatures for CM and at -8 °C for IM.

Discussion

The influence of different icing conditions on UAV airfoils have been shown in detail. Depending on the environmental conditions the ice shape and the impact on aerodynamic performance parameters varies significantly. A comparison between continuous maximum and intermittent maximum conditions reveals different worst case conditions. For CM, the largest aerodynamic penalties can be found close to the freezing temperature at -2 °C and a MVD of 15 µm. For IM conditions, the highest degradation in performance can be found slightly colder temperatures. The most severe conditions is at -6 °C and 20 µm MVD.
As already suggested by [4], the influence of the liquid water content has to be investigated in more detail. It is possible that not the droplet size influences the shape of the accumulated ice but the amount of supercool liquid droplets that impact on the airfoil at a certain time. Therefore, the combination of LWC and the airspeed of the UAV could be a more accurate parameter. An investigation of, firstly, the ice shapes and aerodynamic parameters at a given LWC and temperature and varying MVDs and, secondly, a variation of airspeeds and therefore the Reynolds Number should be conducted. An emphasis therein could be IM conditions due to the higher LWC.
In this paper only monodispersed conditions are investigated. However, in real flight conditions the droplet sizes vary strongly [24]. Using a droplet distribution like the Langmuir D distribution, that describes the variation in cloud droplet diameters, could result in more realistic ice shapes [24]. The Federal Aviation Administration suggests using this distribution with a maximum droplet size of 50 µm for a better determination of impingement limits [24].
Both the numerical generation of ice shapes and evaluation of aerodynamic performance parameters lacks on validation - especially for ice accretion simulations with low Reynolds Numbers. The accuracy of the performance parameters can vary on in the shape of accumulated ice [16]. Further investigations are necessary. In a first step, for different environmental conditions ice shapes should be produced numerically and in an ice wind tunnel, and compared to each other. Parameters could be the ice thickness, the impingement limits, and eventual horn shapes. In a second step, these validated ice shapes could be 3D-printed and attached on the leading edge of a clean airfoil [25]. In a conventional wind tunnel the aerodynamic performance parameters could be tested and compared to the numerical results.
The simulations in this paper have been produced using multishot simulations. In the first step of the conducted investigation, simulations with different numbers of shots were conducted to find the best setting. It showed that the amount of steps has a non-negligible influence on the ice shape and the aerodynamic performance parameters. A more in depth study should be conducted to determine which parameters - numerical, environmental, and regarding the airfoil - have an impact on the number of multishots that should be chosen.
As a UAV is flying through icing conditions it accumulates ice constantly. As seen previously, the iced wing and empennage add additional mass to the UAV and decrease the lift. In real conditions the UAV would have to adjust the AOA the keep flying and would

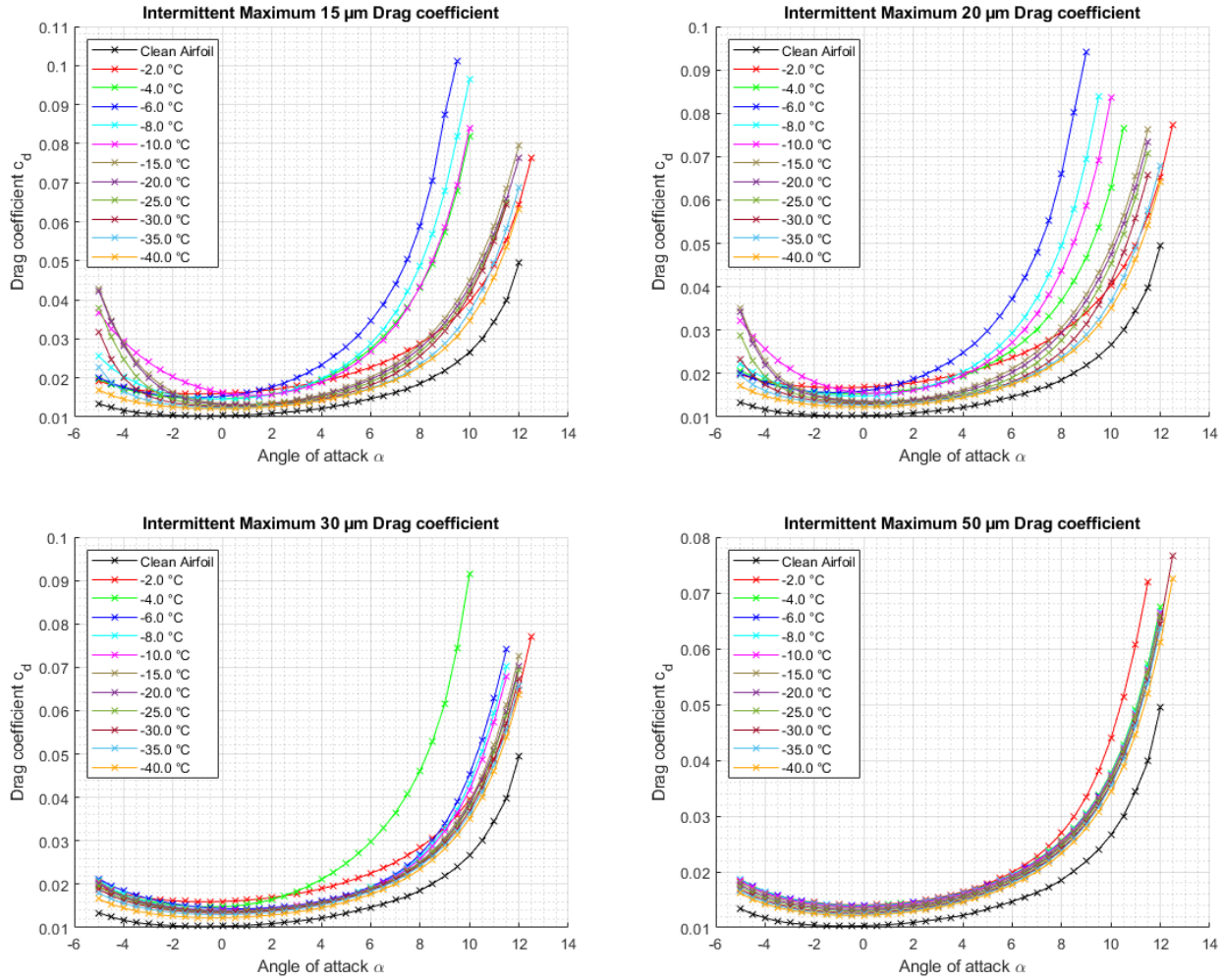

Figure 15: Drag coefficient c_d over the AOA α for the wing in IM conditions.

therefore accumulate ice at different AOAs. In this paper this effect has not been considered. A future investigation could look at the accretion of ice at changing AOAs.

The results presented in this paper extent the knowledge on flights of UAVs in icing conditions. It extents the study of Fajt et al. [4] by investigating more temperatures and MVDs for CM conditions for the RG-15 profile and augments it for IM conditions. A direct comparison is not possible due to different chord length and different AOAs that the ice accretion has been simulated on. The produced results can be used to implement these data into path finding algorithms, flight computer, and flight simulator in icing conditions. Path finding algorithms calculate, in this case depending on the prevailing icing conditions, the most energy efficient way from A to B [26, 27, 28]. Furthermore, these data can be used as a starting point to develop an IPS. Therefore, the results can be used to indicate the most severe icing conditions for both CM and IM. To enable an all weather capable UAV the IPS has to be able to protect wing and empennage in this conditions and are therefore the design point for the system.

Conclusion

This paper investigated the influence of icing conditions on wing and empennage of an UAV by using icing CFD simulations. The icing conditions have been chosen according to FAA CS 25 Appendix C continuous maximum and intermittent maximum icing. For continuous maximum, 54 conditions, for intermittent maximum 88 conditions have been simulated. The study was conducted using three different airfoils. The results include the generated ice shapes, the accumulated ice mass and the impact of aerodynamic performance parameters.

Flying through icing conditions has a severe impact on the flight. The results show decreased lift and reduced stall angles whereas the drag increases. The aerodynamic performance penalties are strongly dependent on the environmental conditions. An icing severity analysis has been conducted and for both icing envelopes two different worst-case conditions were identified. For CM this condition is -2 °C and a MVD of 15 µm, for IM at -6 °C and 20 µm MVD. CM degrades the maximum lift by 37% and increases the drag for an AOA of 4° by 107%. In IM conditions the maximum lift decreases by 35% and drag increases by 103%. The stall angle is reduced from 11° to 7.5° for the worst CM and IM conditions. The increase of the momentum coefficient at already lower AOAs can have a negative impact on the longitudinal stability.

The results can be used to implement these data into path finding algorithms, flight computer, and flight simulator in icing conditions. Furthermore, these data can be used as a starting point to design an ice protection system.

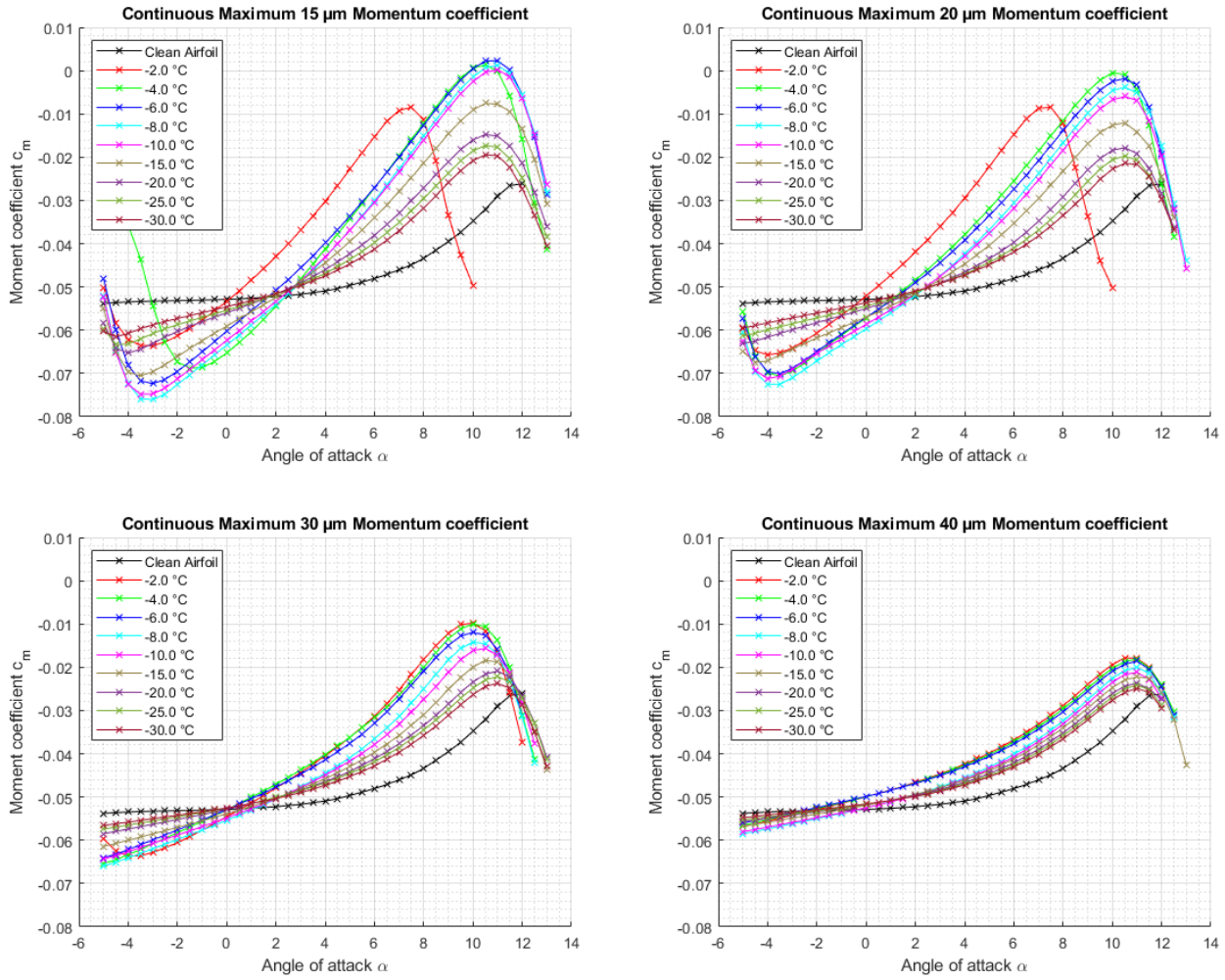

Figure 16: Momentum coefficient c_m over the AOA α for the wing in CM conditions.

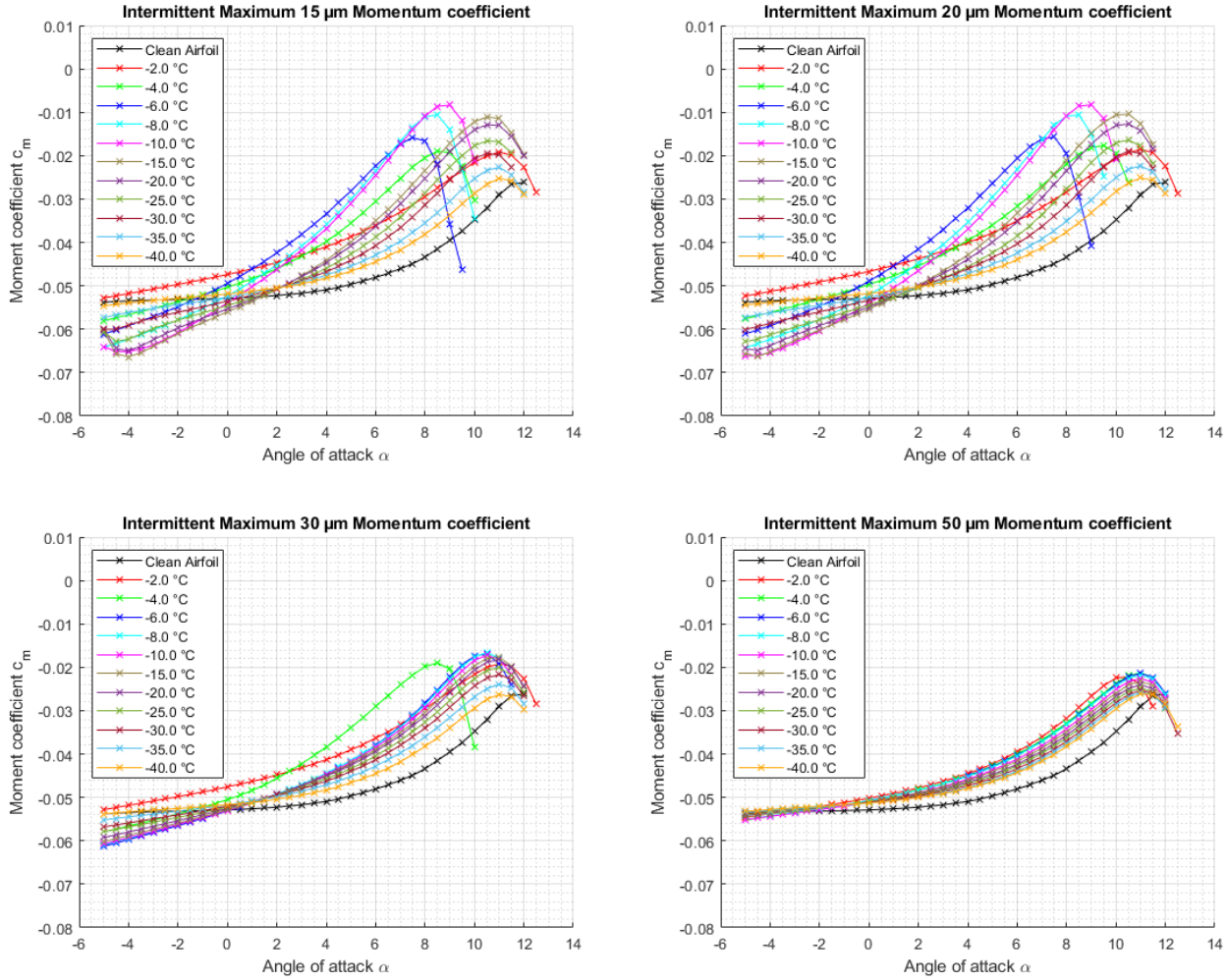

Figure 17: Momentum coefficient c_m over the AOA α for the wing in IM conditions.

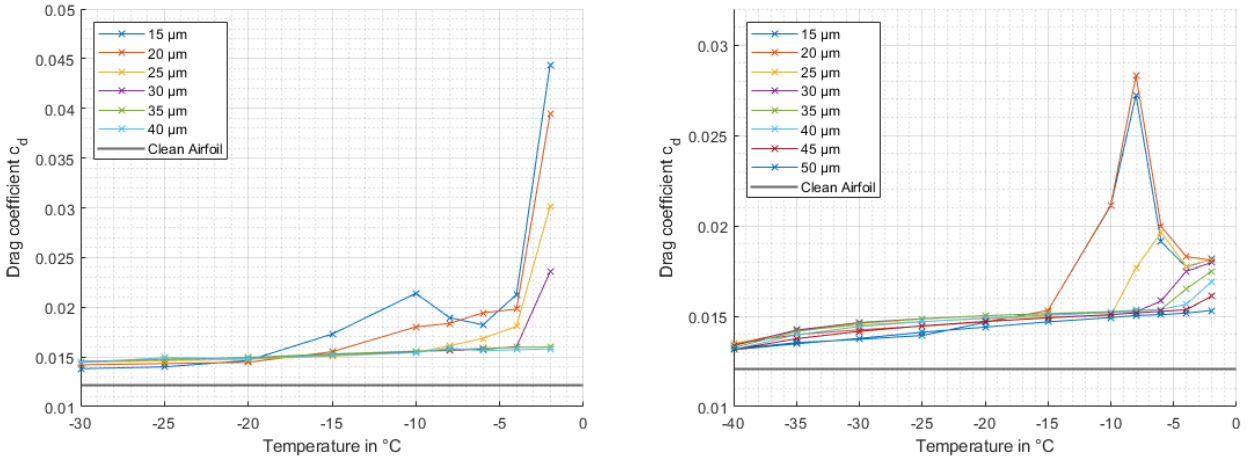

Figure 18: Drag coefficient c_d for ice accumulated on the rudder at different temperatures for CM and IM conditions.

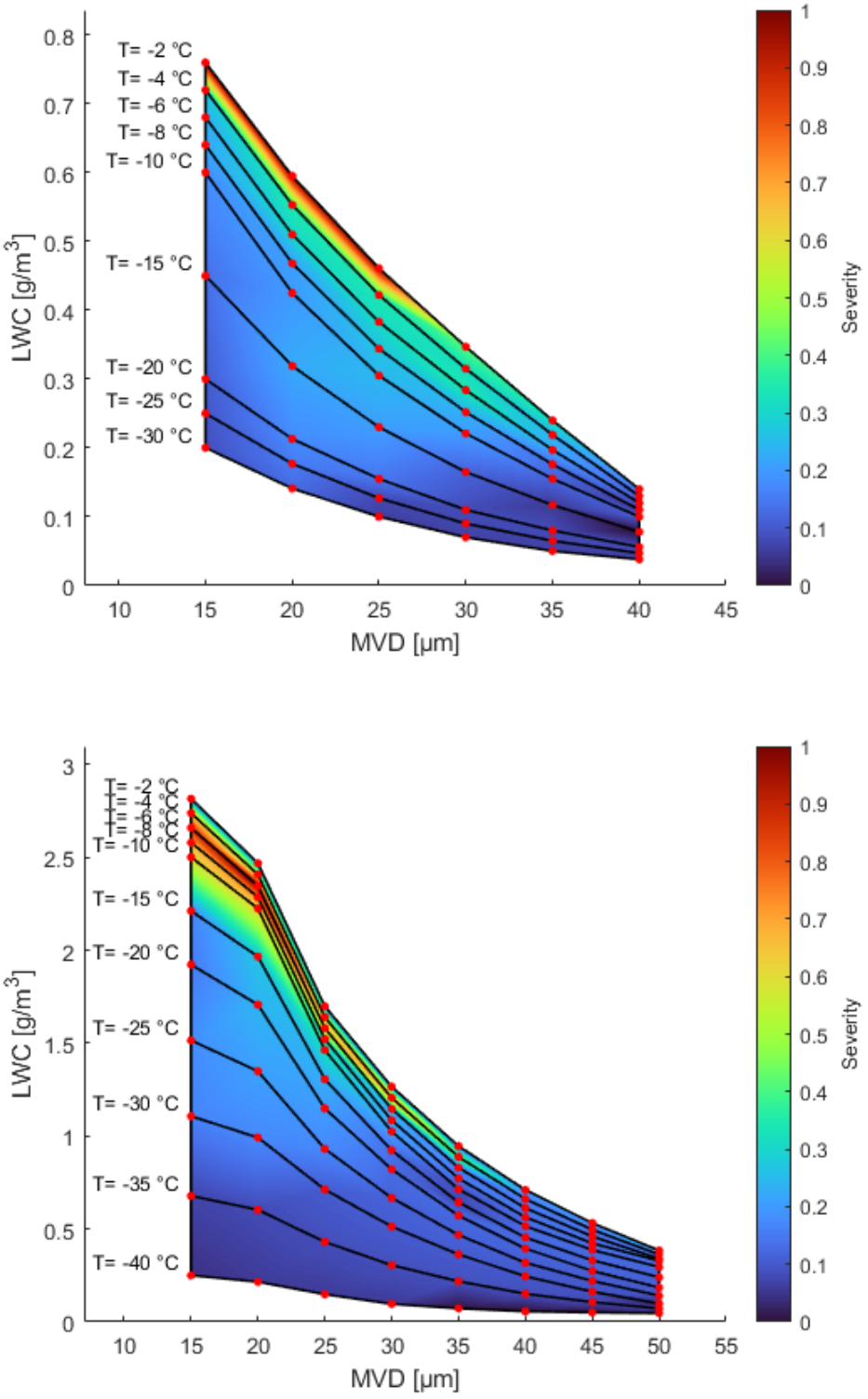

Figure 19: Icing severity index for the wing in CM (top) and IM (bottom) conditions.

References

1. Federal Aviation Administration, "FAA National Forecast 2022-2042," Report, 2022.

2. R. Hann and T. A. Johansen, "Unsettled Topics in Unmanned Aerial Vehicle Icing," *SAE EDGE Research Report*, 2020.

3. R. Hann, "Atmospheric Ice Accretions, Aerodynamic Icing Penalties, and Ice Protection Systems on Unmanned Aerial Vehicles," Ph.D. dissertation, Norwegian University of Science and Technology, 2020.

4. N. Fajt, R. Hann, and T. Lutz, "The Influence of Meteorological Conditions on the Icing Performance Penalties on a UAV Airfoil," *Proceedings of the 8th European Conference for Aeronautics and Space Sciences*, 2019.

5. Y. Cao, W. Tan, and Z. Wu, "Aircraft icing: An ongoing threat to aviation safety," *Aerospace Science and Technology*, vol. 75, pp. 353–385, 2018.

6. Z. Goraj, "An Overview of the Deicing and Anti-icing Technologies with Prospects for the Future," *24th International Congress of the Aeronautical Sciences*, 2004.

7. K. L. Sørensen, "Autonomous Icing Protection Solution for Small Unmanned Aircraft," Ph.D. dissertation, Norwegian University of Science and Technology, 2016.

8. R. Hann, A. Enache, M. C. Nielsen, B. N. Stovner, J. van Beeck, T. A. Johansen, and K. T. Borup, "Experimental Heat Loads for Electrothermal Anti-Icing and De-Icing on UAVs," *Aerospace Deicing and Anti-Icing of Aircraft*, vol. 2, 2021.

9. B. C. Bernstein, C. A. Wolff, and F. McDonough, "An inferred climatology of icing conditions aloft, including supercooled large drops. Part I: Canada and the continental United States," *Journal of applied meteorology and climatology*, vol. 46, no. 11, pp. 1857–1878, 2007.

10. B. C. Bernstein and C. L. Bot, "An inferred climatology of icing conditions aloft, including supercooled large drops. Part II: Europe, Asia, and the globe," *Journal of applied meteorology and climatology*, vol. 48, no. 8, pp. 1503–1526, 2009.

11. UBIQ AEROSPACE, "UAV Atmospheric Icing Limitations - Climate report for Norway and surrounding regions," Report, 2021.

12. Federal Aviation Administration, "Part I — Atmospheric Icing Conditions," *14 CFR 25 Appendix 25*, 2016.

13. M. Bragg, A. Broeren, and L. Blumenthal, "Iced-airfoil aerodynamics," *Progress in Aerospace Science*, vol. 41, pp. 323–362, 2005.

14. S. E. Bansmer, *Aircraft Icing - A challenging problem of fluid mechanics*, 1st ed. Göttingen: Cuvillier Verlag, 2020.

15. Maritime Robotics, "The Falk," https://www.maritimerobotics.com/falk, Accessed: 20.11.2022.

16. R. Hann, R. J. Hearst, L. R. Sætran, , and T. Bracchi, "Experimental and Numerical Icing Penalties of an S826 Airfoil at Low Reynolds Numbers," *Aerospace*, vol. 7(4), 46, 2020.

17. R. Hann, "UAV Icing: Comparison of LEWICE and FENSAP-ICE for Anti-Icing Loads," AIAA Scitech 2019 Forum, Tech. Rep., 2019, https://doi.org/10.2514/6.2019-1286.

18. G. S. Baruzzi, W. G. Habashi, G. Guèvremont, and M. M. Hafez, "A Second Order Finite Element Method for the Solution of the Transonic Euler and Navier-Stokes Equations," *Int. J. Numer. Methods Fluids*, vol. 20, pp. 671–693, 1995.

19. Y. Bourgault, Z. Boutanios, and W. Habashi, "3D Eulerian Droplets Impingement Using FENSAP-ICE, Part I: Model, Algorithms and Validation," *AIAA Journal of Aircraft*, vol. 37, pp. 95–103, 2000.

20. Ansys Inc., *Ansys FENSAP-ICE User Manual*, 2022.

21. Y. Bourgaul, H. Beaugendre, and W. Habashi, "Development of a Shallow-Water Icing Model in FENSAP-ICE," *Journal of Aircraft*, vol. 37(4), 2000.

22. I. Ozcer, D. Switchenko, G. S. Baruzzi, and J. Chen, "Multi-Shot Icing Simulations with Automatic Re-Meshing," Conference: International Conference on Icing of Aircraft, Engines, and Structures, Tech. Rep., 2019, https://doi.org/10.4271/2019-01-1956.

23. Ansys Inc., *ANSYS FENSAP-ICE Tutorial Guide*, 2021.

24. Federal Aviation Administration, "Aircraft Ice Protection - Advisory Circular No: 20-73A," Advisory Circular, 2006.

25. J. W. Oswald, A. Enache, R. Hann, G. Glabeke, and T. Lutz, "UAV Icing: Experimental and Numerical Study of Glaze Ice Performance Penalties on an RG-15 Airfoil," AIAA SCITECH 2022 Forum, Tech. Rep., 2021, https://doi.org/10.2514/6.2022-1976.

26. M. Cheung and R. Hann, "UAV Icing: Icing Cases for Validation of Particle Swarm Path Planning Method," SAE Technical Paper, Tech. Rep., 2023, (in press).

27. E. F. L. Narum, R. Hann, and T. A. Johansen, “Optimal Mission Planning for Fixed-Wing UAVs with Electro-Thermal Icing Protection and Hybrid-Electric Power Systems,” 2020 International Conference on Unmanned Aircraft Systems, Tech. Rep., 2020, https://doi.org/10.1109/ICUAS48674.2020.9214054.

28. A. R. Hovenburg, F. A. de Alcantara Andrade, R. Hann, C. D. Rodin, T. A. Johansen, and R. Storvold, “Long-Range Path Planning Using an Aircraft Performance Model for Battery-Powered sUAS Equipped With Icing Protection System,” IEEE Journal on Miniaturization for Air and Space Systems, Tech. Rep., 2020, https://doi.org/10.1109/JMASS.2020.3003833.

Contact Information

Markus Lindner, Ph.D. student
markus.lindner@ntnu.no

Joachim Wallisch, Ph.D. student
joachim.wallisch@ntnu.no

Richard Hann, Ph.D.
richard.hann@ntnu.no

Acknowledgments

The work is partly sponsored by the Research Council of Norway through the Centre of Excellence funding scheme, project number 223254, AMOS, and the ITKPLUSS project number 316425. The numerical simulations were performed on resources provided by the National Infrastructure for High Performance Computing and Data Storage in Norway (UNINETT Sigma2) on the Fram supercomputer, under project code NN9613K Notur/NorStore. Furthermore, the authors would like to thank Ansys, Inc. for providing the initial version of the automation script and Maritime Robotics for providing the PX-31 Falk UAV data.

Abbreviations

AOA	angle of attack
CFD	computational fluid dynamics
CM	continuous maximum
FAA	Federal Aviation Administration
IM	intermittent maximum
IPS	ice protection system
LWC	liquid water content
MVD	median volumetric diameter
RANS	reynolds-averaged Navier–Stokes equations
UAV	unmanned aerial vehicle

APPENDIX A

Elevator ice shapes for continuous maximum

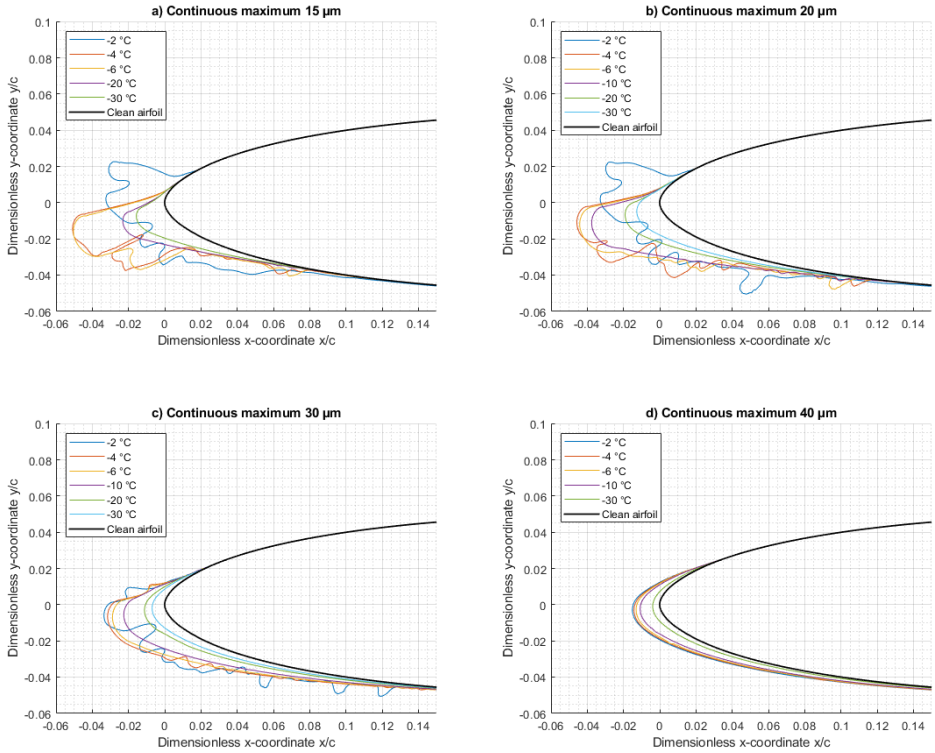

Figure 20: Elevator ice shapes for CM conditions

Elevator ice shapes for intermittent maximum.

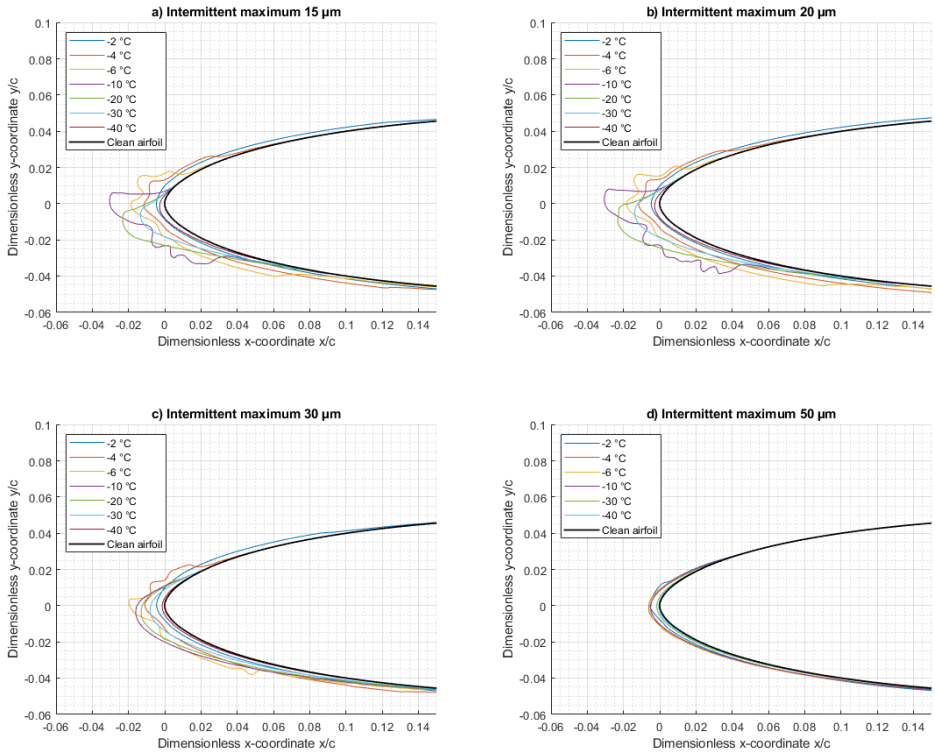

Figure 21: Elevator ice shapes for IM conditions.

Rudder ice shapes for continuous maximum

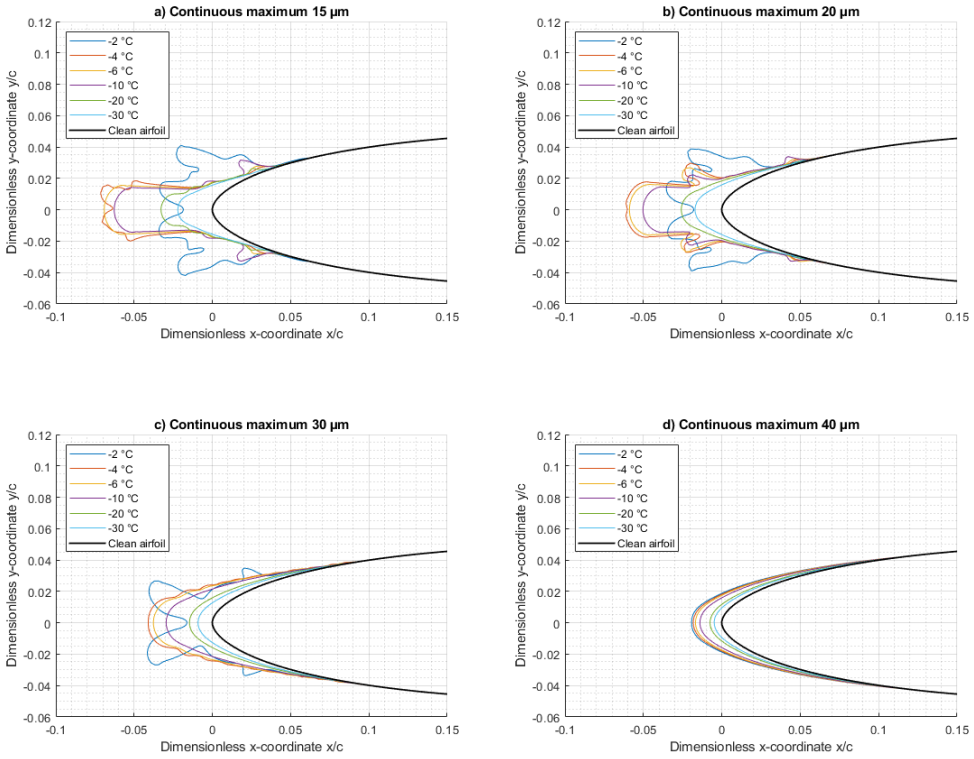

Figure 22: Rudder ice shapes for CM conditions.

Rudder ice shapes for intermittent maximum

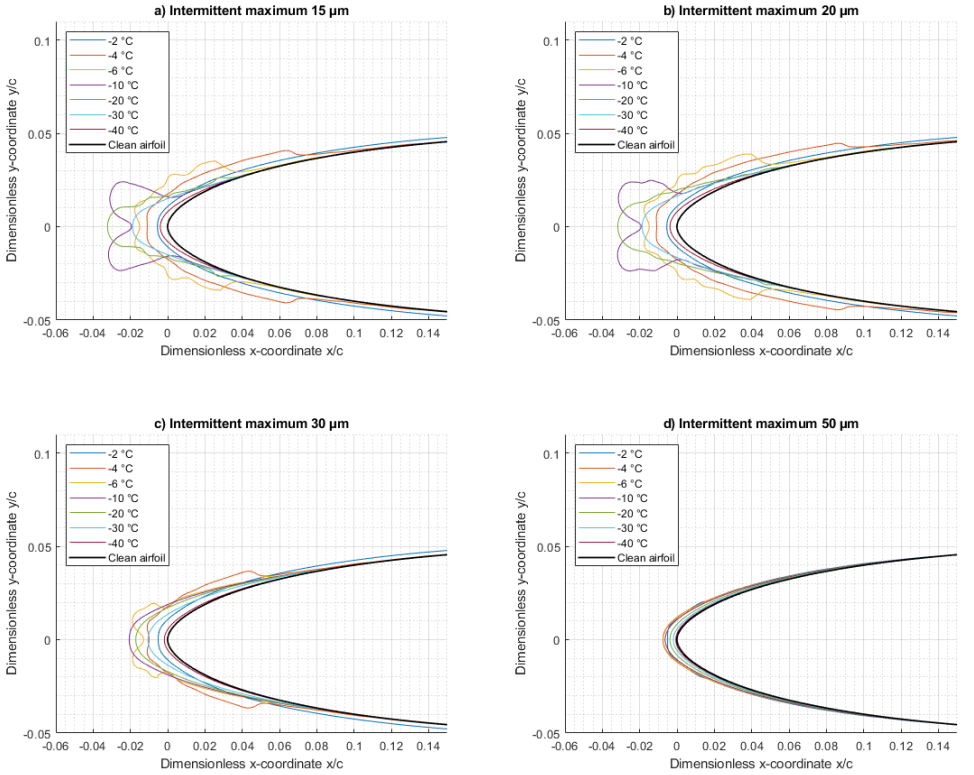

Figure 23: Rudder ice shapes for IM conditions.

Additional lift coefficients for wing

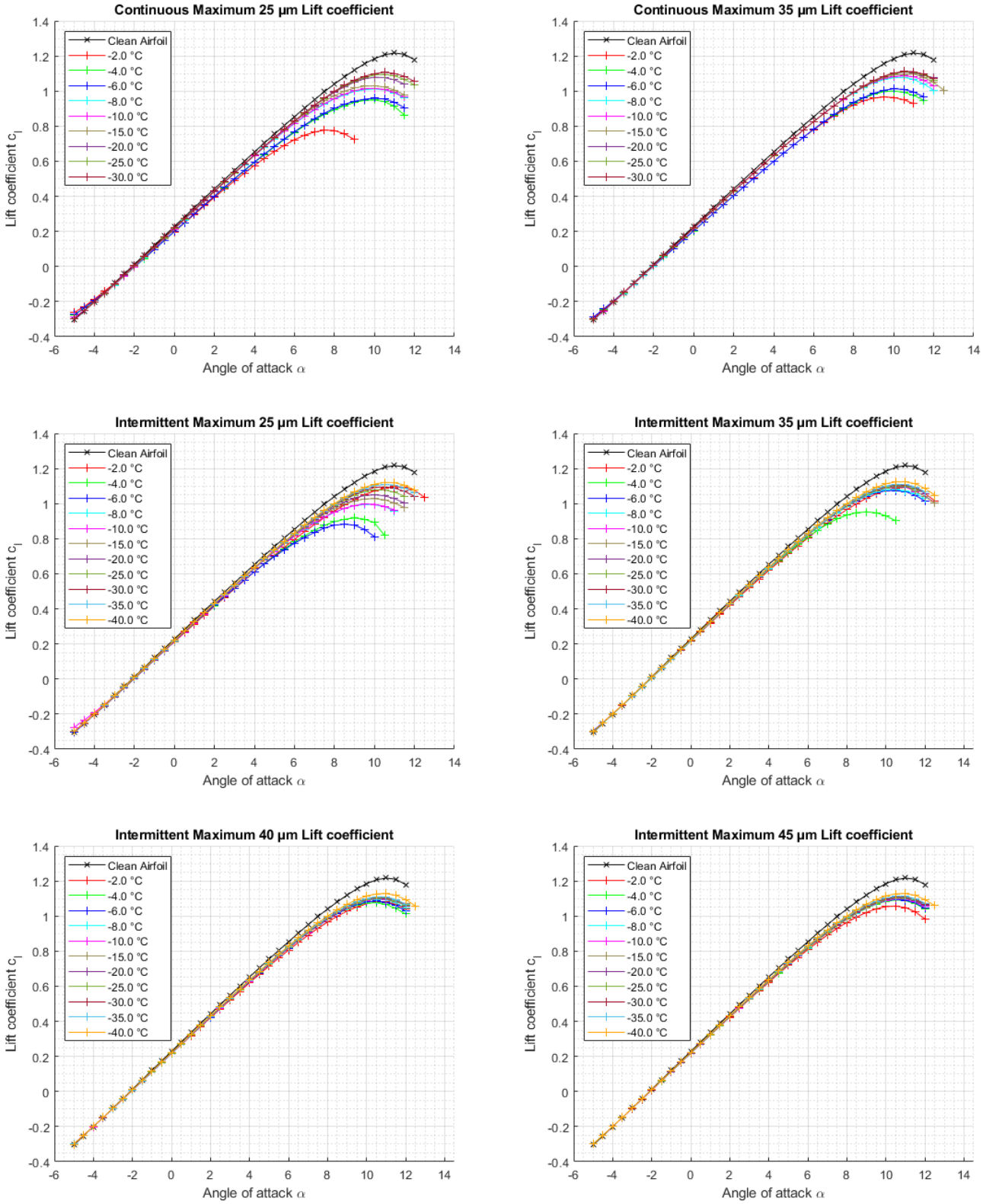

Figure 24: Additional lift coefficient plots of the wing in CM and IM conditions.

Lift coefficients elevator for continuous maximum

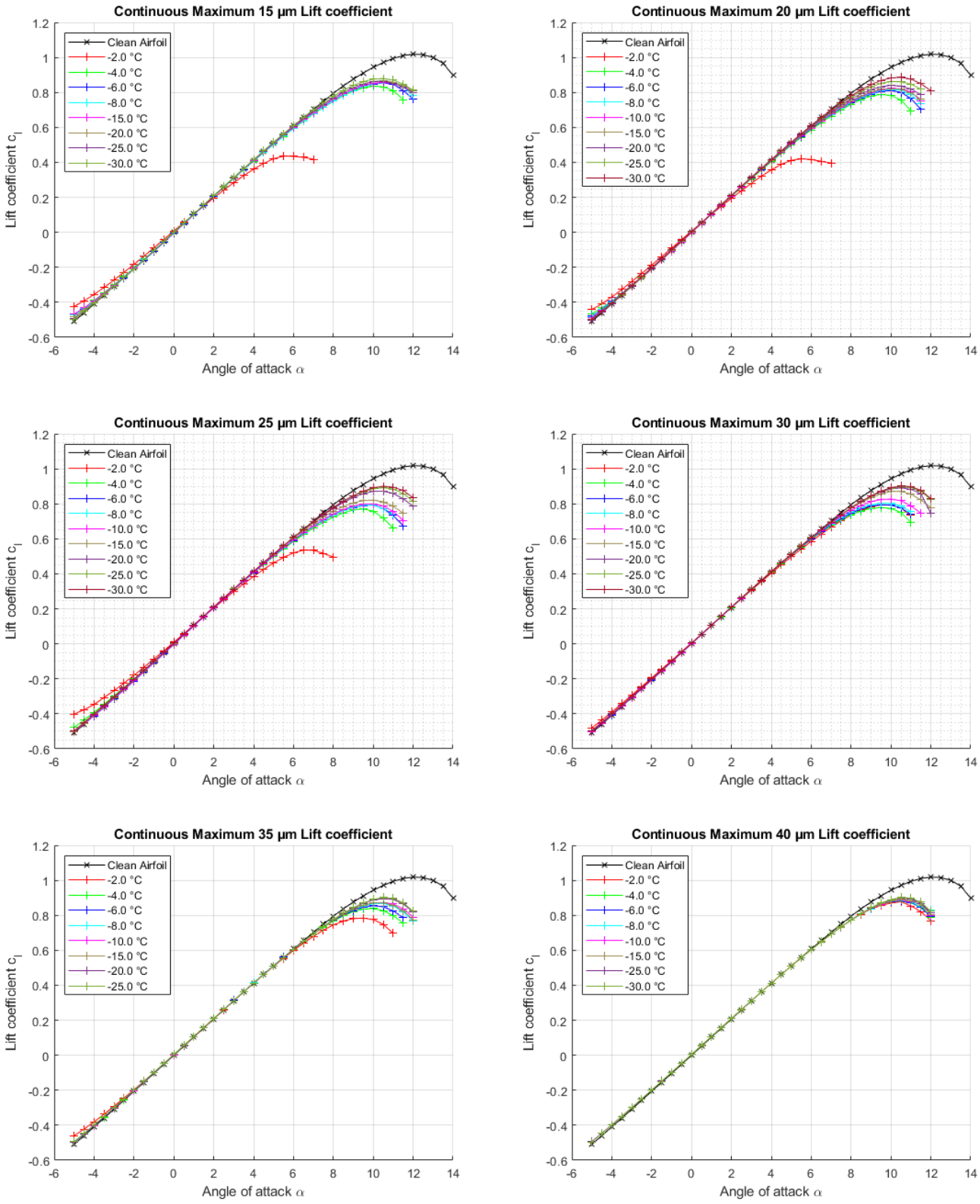

Figure 25: Lift coefficients of the elevator in CM conditions.

Lift coefficients elevator for intermittent maximum

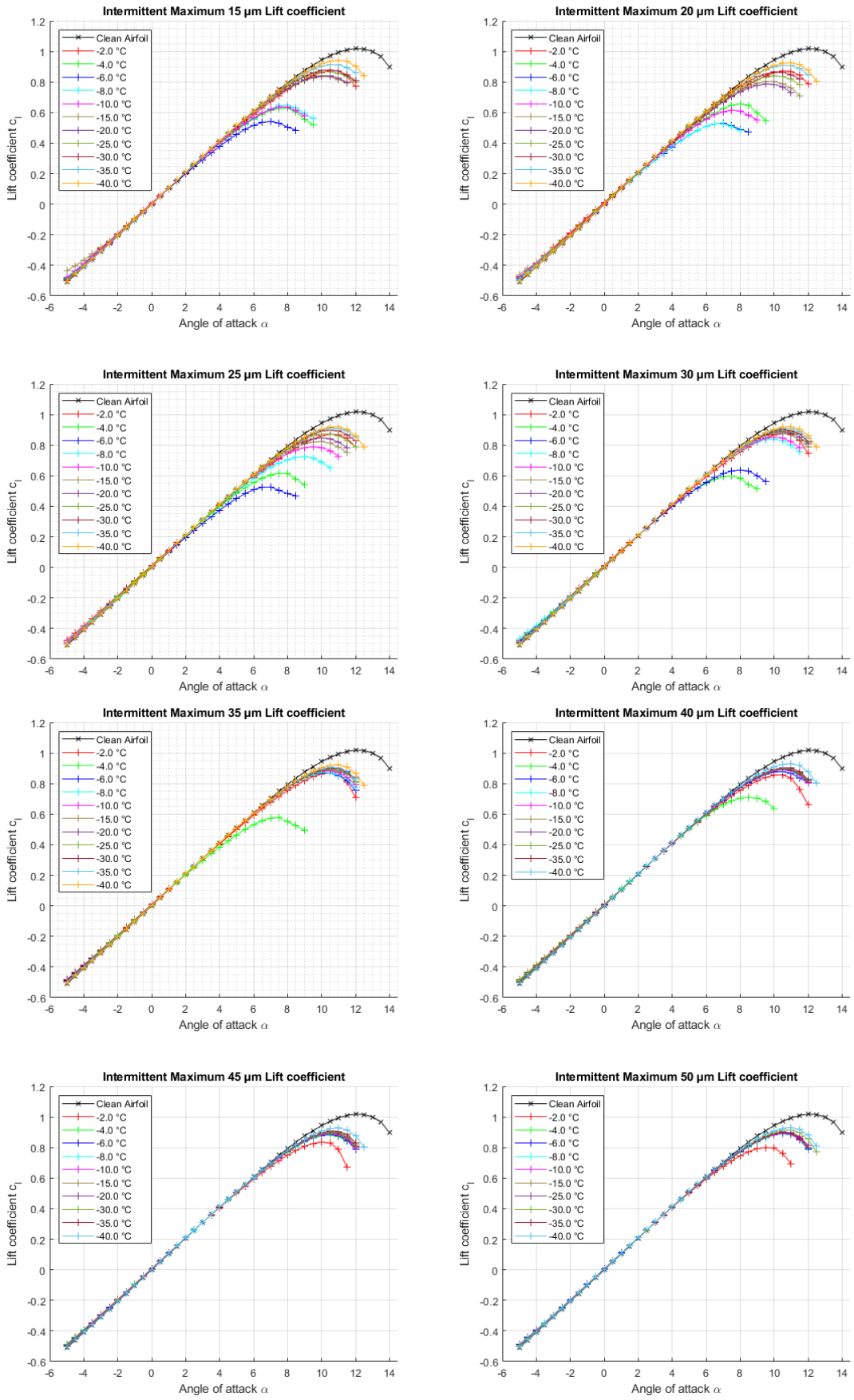

Figure 26: Lift coefficients of the elevator in IM conditions.

Additional drag coefficients for wing

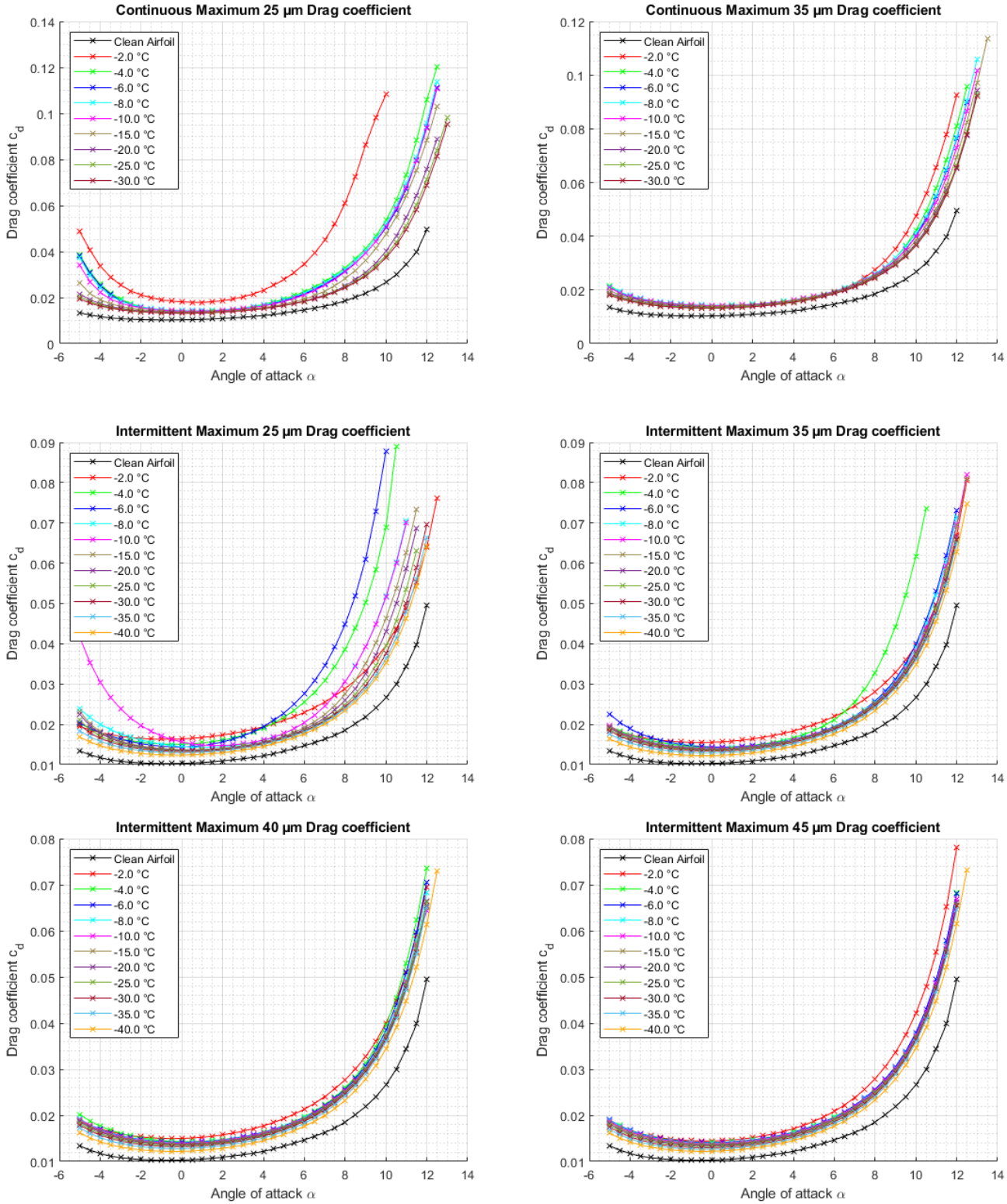

Figure 27: Additional drag coefficient plots of the wing in CM and IM conditions.

Drag coefficients elevator for continuous maximum

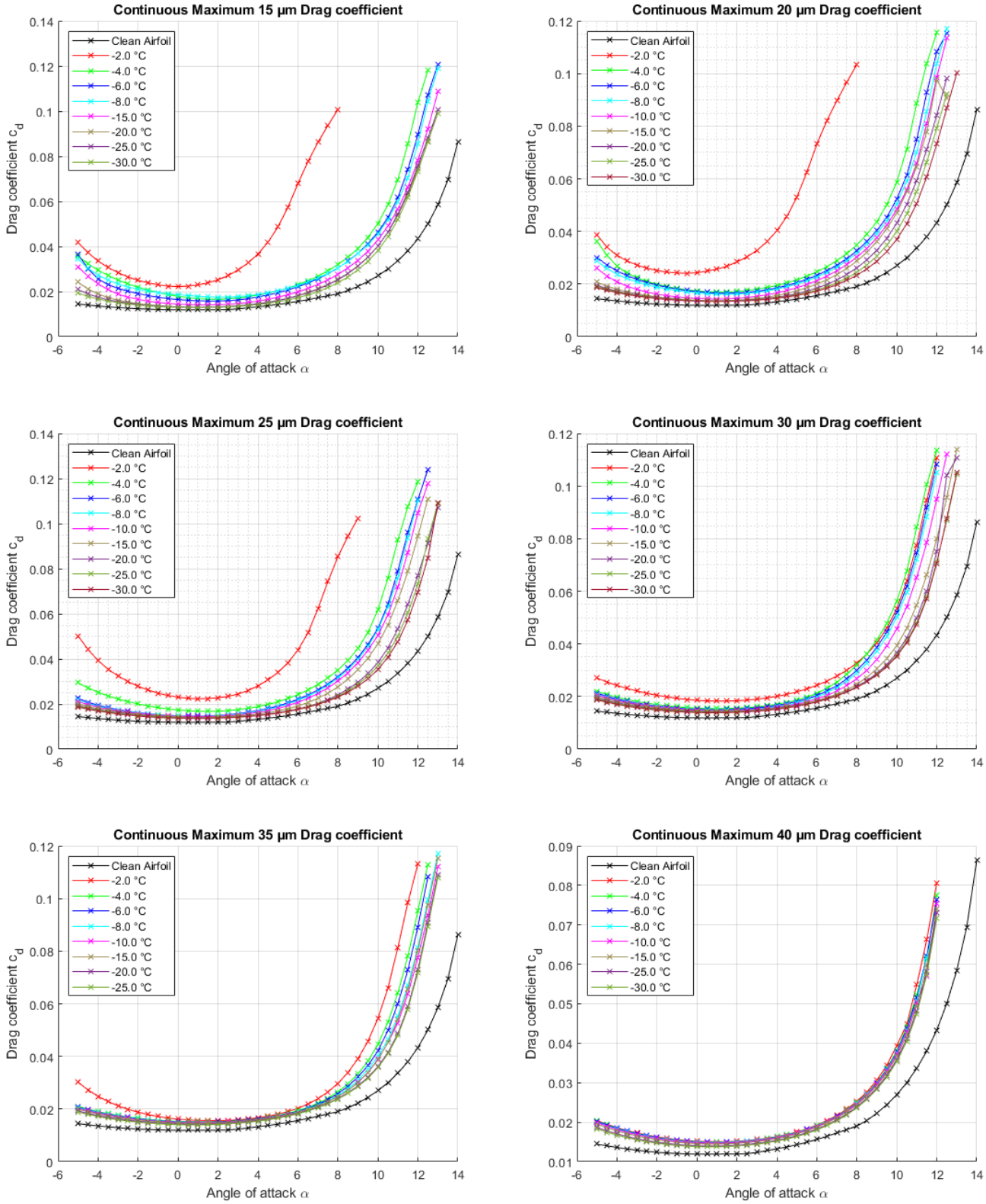

Figure 28: Drag coefficients of the elevator in CM conditions.

Drag coefficients elevator for intermittent maximum

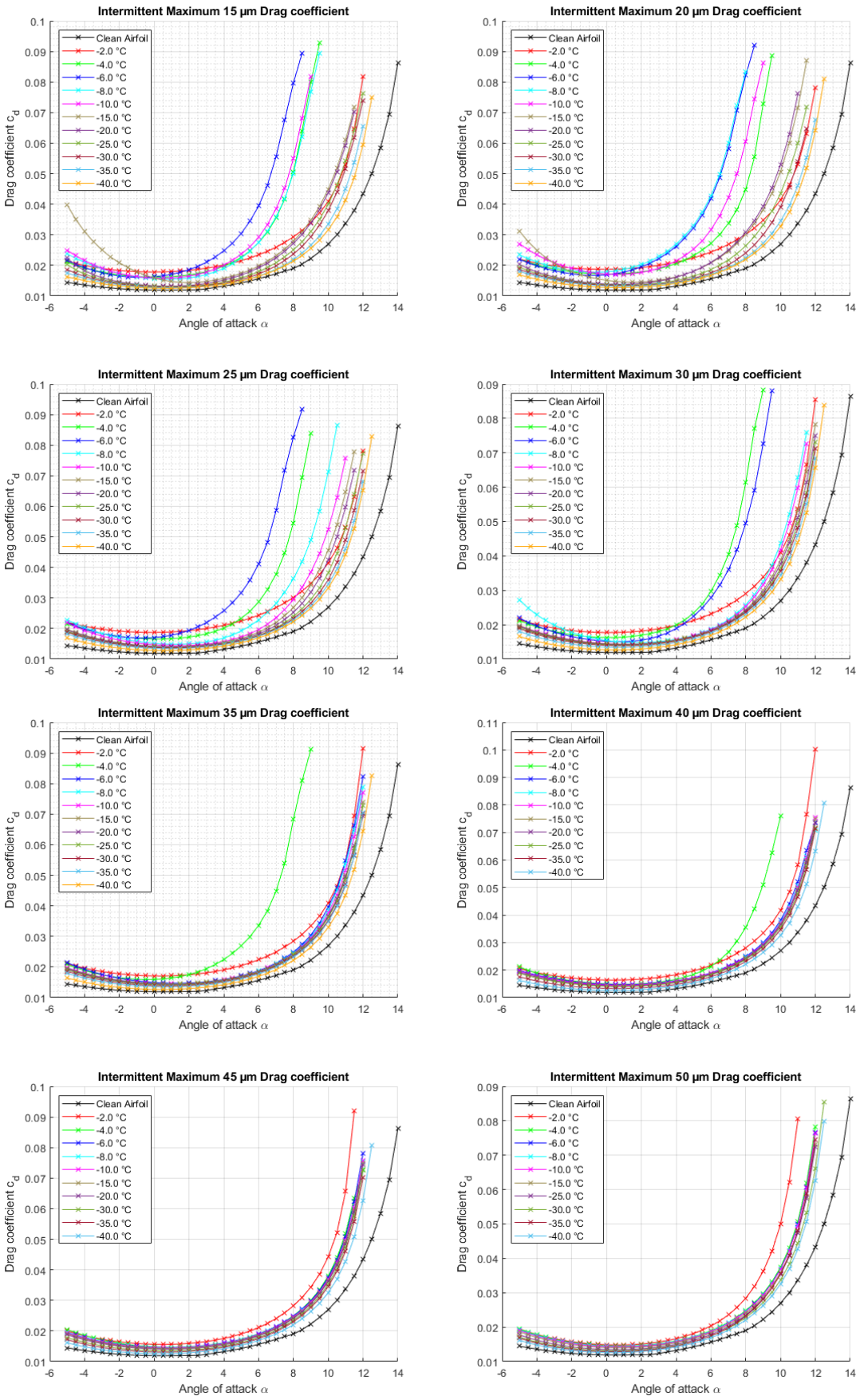

Figure 29: Drag coefficients of the elevator in IM conditions.

Additional momentum coefficients for wing

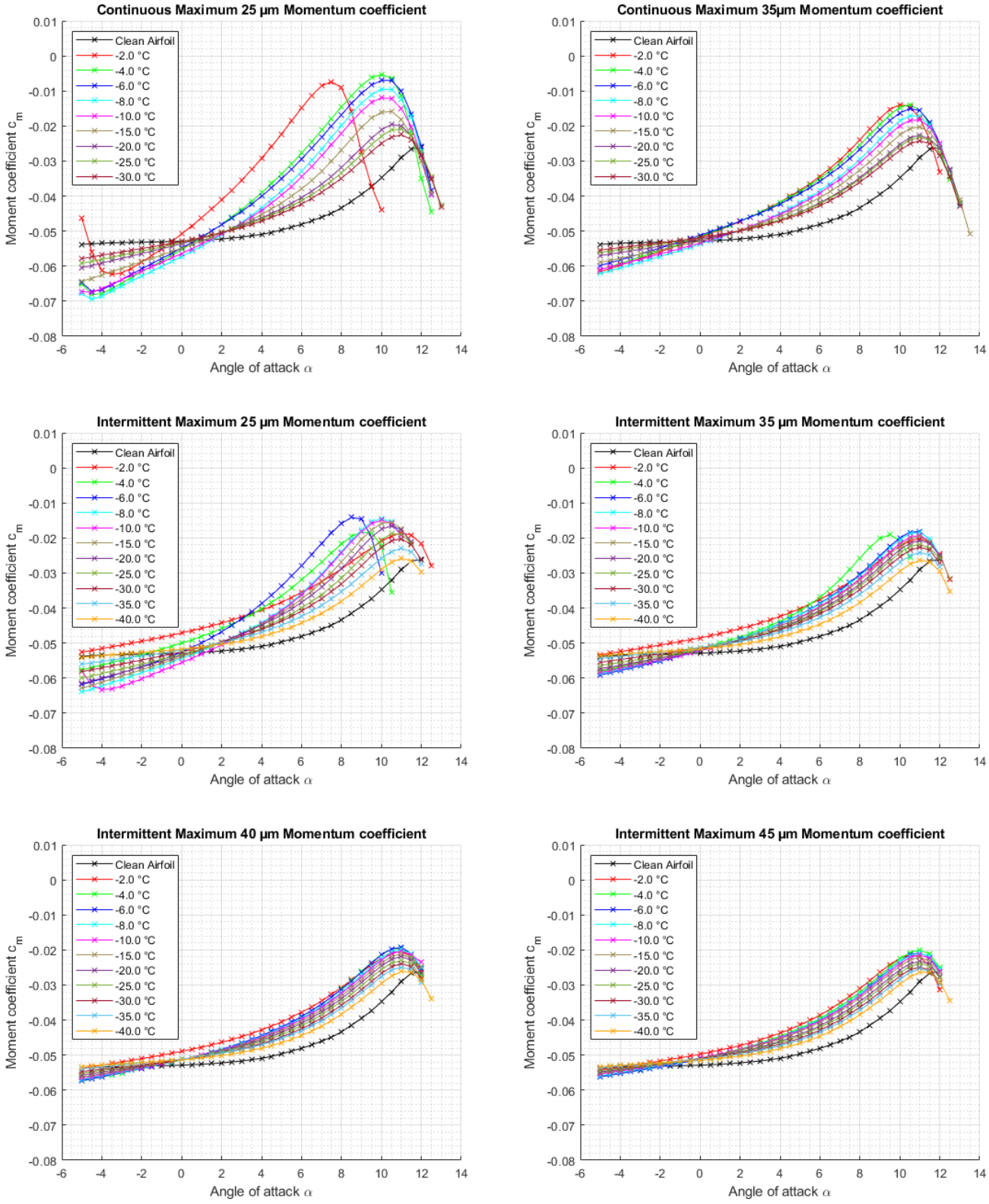

Figure 30: Additional momentum coefficient plots of the wing in CM and IM conditions.

Momentum coefficients elevator for continuous maximum

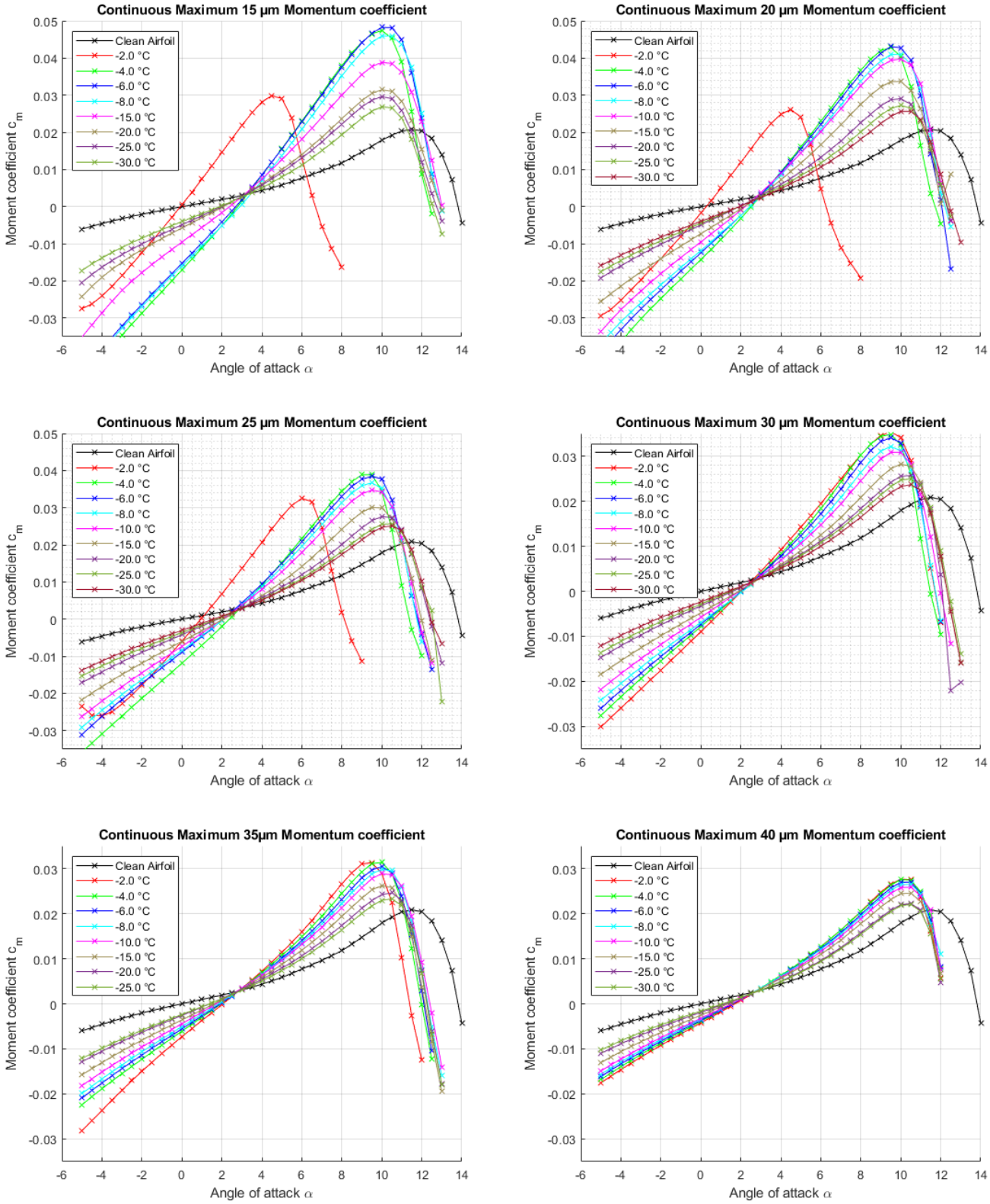

Figure 31: Momentum coefficients of the elevator in CM conditions.

Momentum coefficients elevator for intermittent maximum

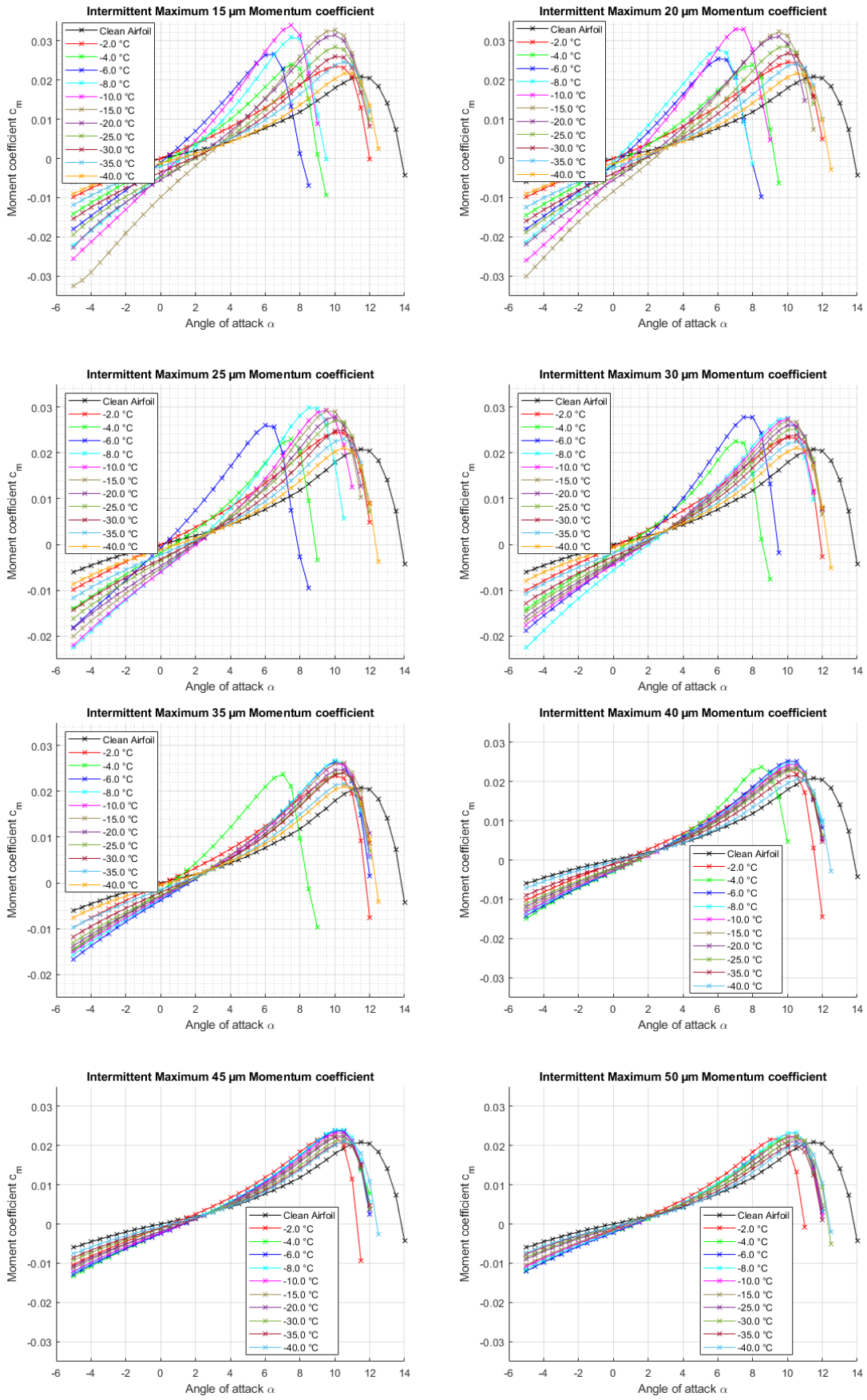

Figure 32: Momentum coefficients of the elevator in IM conditions.

Momentum coefficients elevator for intermittent maximum

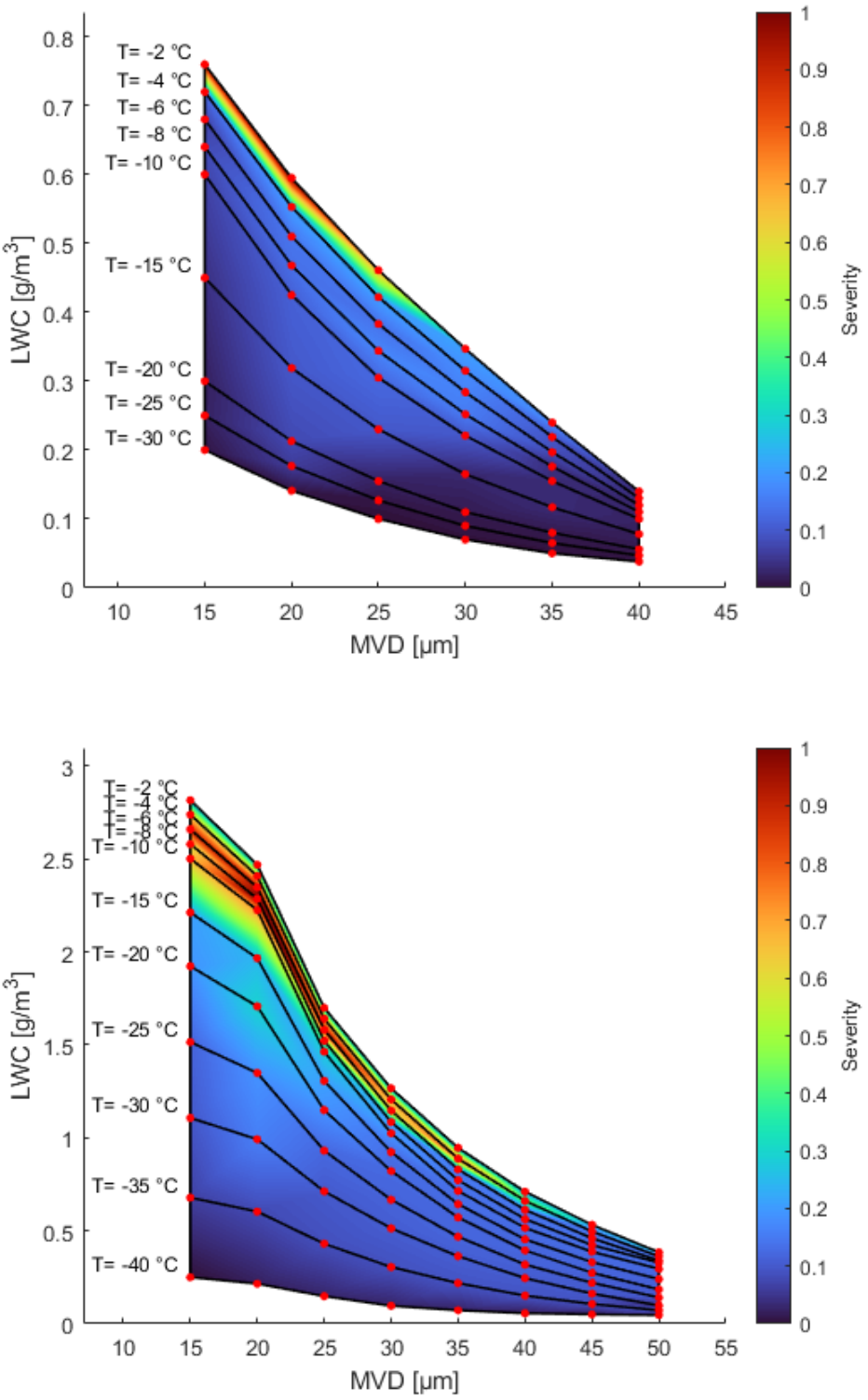

Figure 33: Icing severity index for the elevator in CM (top) and IM (bottom) conditions.

APPENDIX B

C_l over C_d for the wing in continuous maximum conditions

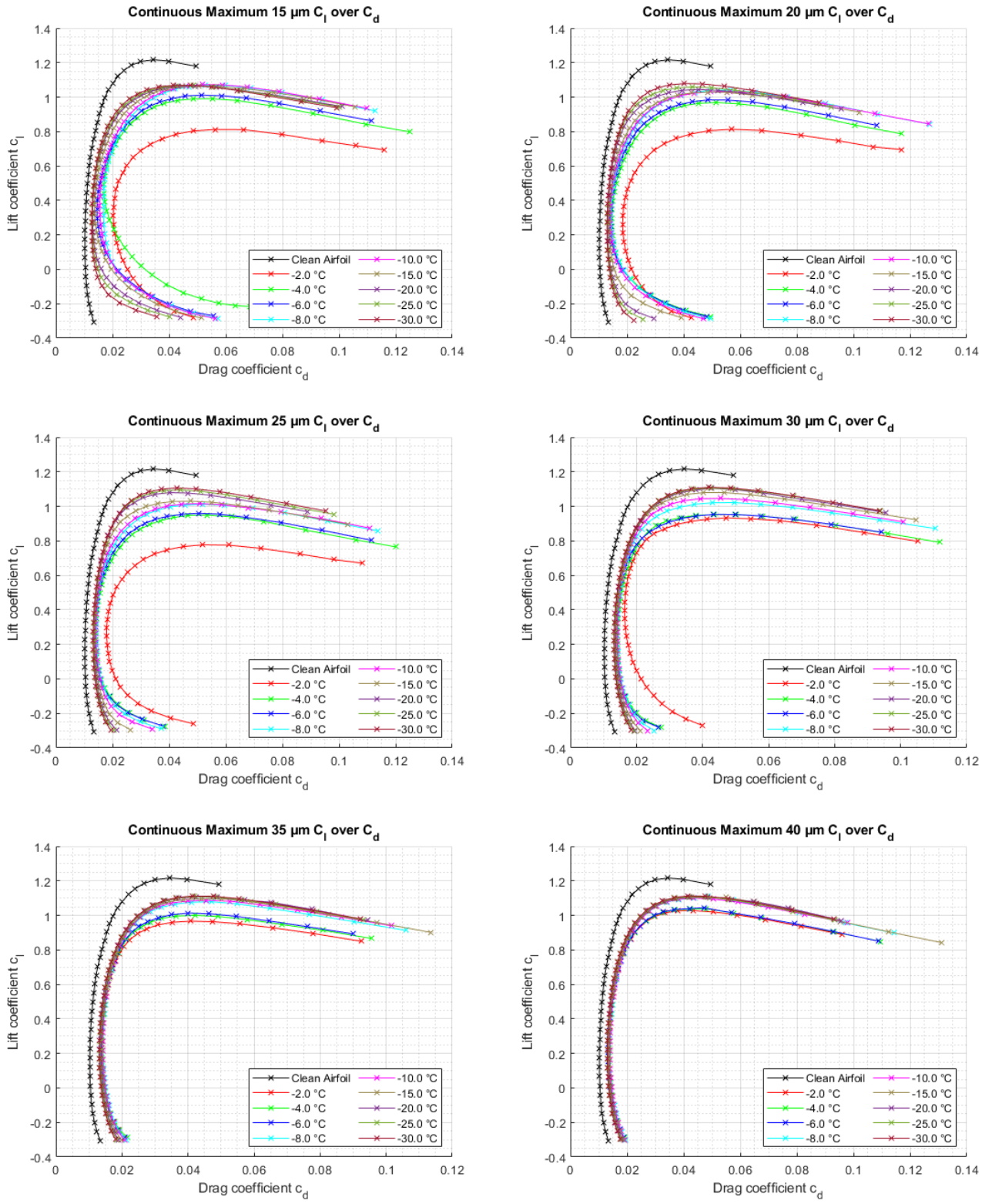

Figure 34: C_l over C_d of the wing in CM conditions.

C_l over C_d for the wing in continuous maximum conditions

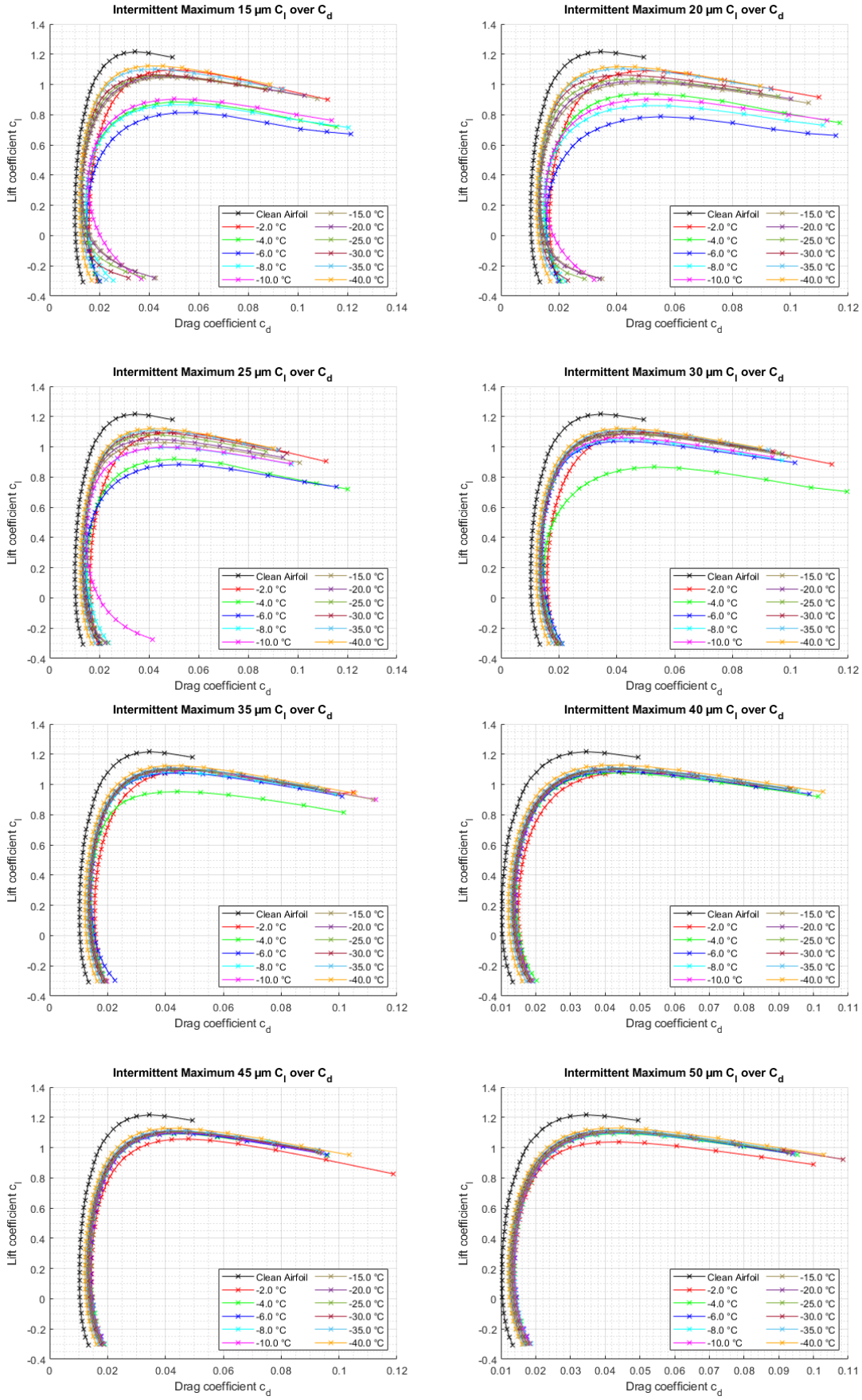

Figure 35: C_l over C_d for the wing in IM conditions.

APPENDIX C

Beading height for the wing at −10 °C and 15 µm MVD

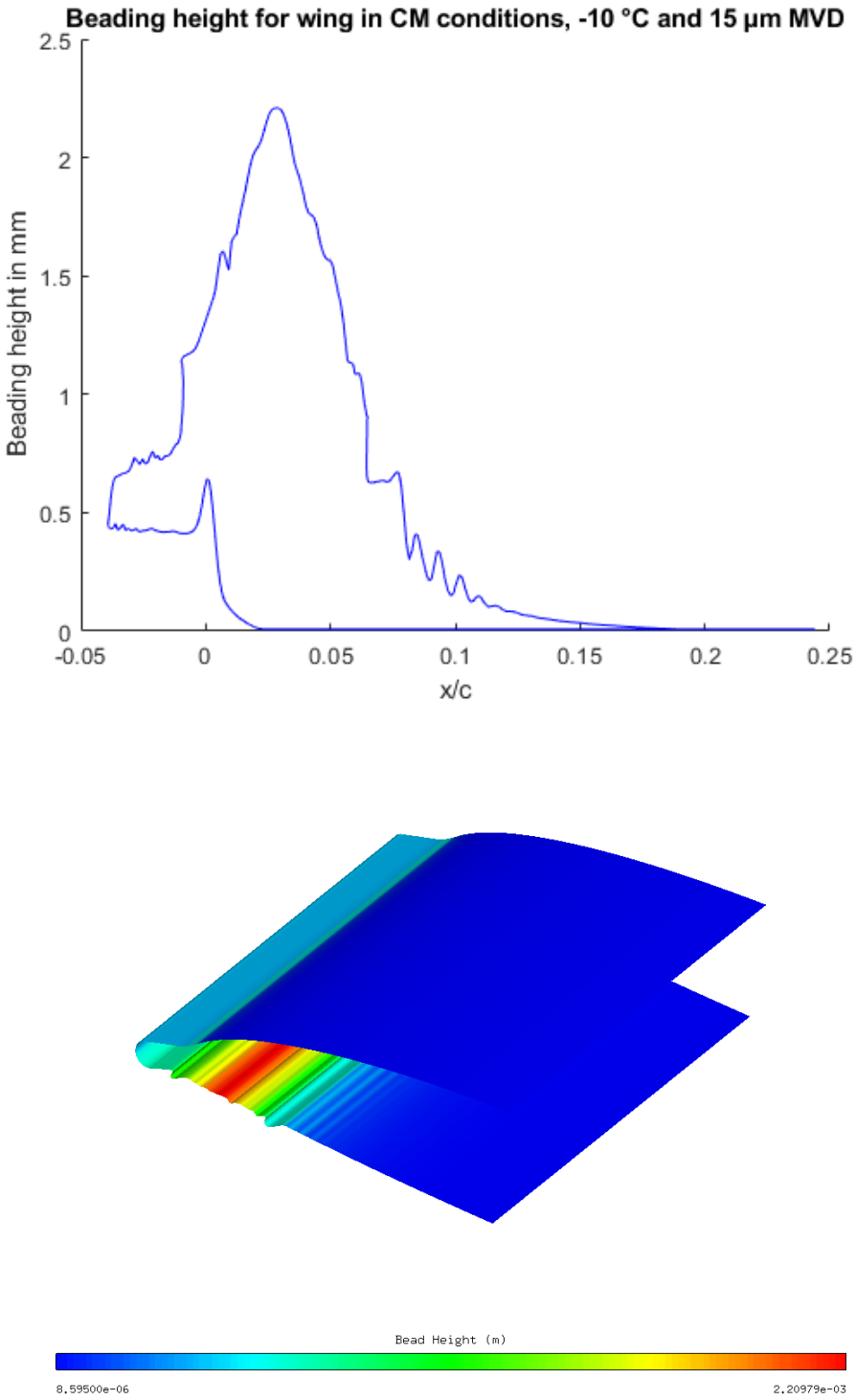

Figure 36: Beading height for wing at CM conditions at −10 °C and 15µm MVD